Higher Order Trapped Lee Waves in the Stratosphere

Johnathan J. Metz

A thesis
submitted in partial fulfillment of the
requirements for the degree of

Master of Science

University of Washington

2018

Committee:

Dale R. Durran

Christopher S. Bretherton

Kyle C. Armour

Program Authorized to Offer Degree:
Atmospheric Sciences

University of Washington

Abstract

Higher Order Trapped Lee Waves in the Stratosphere

Johnathan J. Metz

Chair of the Supervisory Committee:
Professor Dale R. Durran
Atmospheric Sciences

Wave activity with maximum amplitude in the stratosphere downstream of major mountain ranges has previously been explained as a result of wave breaking inducing secondary wave generation in the stratosphere (Vadas et al., 2003) or the vertical propagation of low-amplitude waves from below. However, theoretical results as early as Scorer (1949) and Corby and Wallington (1956) have posited the existence of higher-order trapped wave modes. Although the higher-order modes in these studies were confined to the troposphere due to the studies' theoretical setup, Corby and Wallington (1956) demonstrate that the level of maximum amplitude for higher-order modes in a two-layer atmosphere with constant Scorer parameter in each layer is higher in the vertical than that of lower-order modes. The increased height of the level of maximum amplitude raises the possibility of higher-order modes with significant amplitude in the stratosphere. However, while higher-order trapped wave modes are theoretically predicted to exist, they are not known to have been observed in the real atmosphere or simulated in realistic numerical models.

The DEEPly Propagating Gravity WAVE campaign (DEEPWAVE) was conducted over New Zealand from 29 May 2014 to 27 July 2014 (Fritts et al., 2015). Immediately after the end of the intensive observing period, on 28 July, a strong event occurred. Model simulations of this event revealed unusual wave activity in the stratosphere. These waves were located downstream of the topography, like a trapped wave, but were oriented from south to north,

in contrast to the more typical southwest-northeast orientation paralleling the crest of the Southern Alps.

Vertical cross-sections of the unusual waves exhibit a nodal structure consistent with that of a higher-order trapped wave mode. Solutions to the two-dimensional, linear, Boussinesq wave equation for a horizontally homogeneous sounding derived from the 28 July case include higher-order modes supported by the zonal wind which have large amplitude in the stratosphere. These higher-order modes are trapped by very strong westerly winds in the upper stratosphere. In contrast, the cross-mountain wind component is not strong enough in the stratosphere to trap the same wave mode in a crest-parallel orientation. These waves are reproducible in both two- and three-dimensional compressible numerical models with both idealized and realistic terrains, and therefore provide a plausible explanation for the wave activity in the stratosphere.

TABLE OF CONTENTS

LIST OF FIGURES

LIST OF TABLES

ACKNOWLEDGMENTS

First and foremost, I would like to thank my advisor, Dr. Dale Durran, for his brilliant scientific expertise and patient guidance throughout the last several years.

I would also like to thank my undergraduate research advisor, Dr. Gretchen Mullendore, who was willing to allow a young, immature sophomore into her research group and mentor him for the next two years. I wouldn't be here at UW without her guidance and support.

In addition, Dr. Mike Fiorino of the NOAA Earth System Research Laboratory in Boulder, Colorado was an exceptional internship mentor during the summer of 2014. He fostered my interest in model development and theoretical work that has persisted to this day.

My first year of graduate school was supported by the American Meteorological Society's Graduate Fellowship.

Finally, I would like to thank my family for all of their support and assistance throughout the years.

DEDICATION

To Grandpa, for providing the inspiration that brought me here.

"What you leave behind is not what is engraved in stone monuments, but what is woven into the lives of others." – Pericles

Chapter 1

INTRODUCTION

Atmospheric waves are a fundamental mode of atmospheric motion. These waves appear at all scales, from Rossby waves at synoptic and global scales, to gravity waves in the mesoscale. Furthermore, waves can exert influence across scales. For example, Rossby waves determine the large scale basic state that influences the generation and propagation of gravity waves, and gravity waves can deposit or extract momentum from the mean flow when they break (Eliassen and Palm, 1960). Therefore, improving our understanding of the dynamics of atmospheric waves at any scale is important to furthering our understanding of the broader atmosphere.

Understanding of gravity waves in particular is important for aviation meteorology applications. As many airline passengers flying over mountain ranges have noticed, turbulence is often stronger over mountain ranges than over flat topography. This is due in no small part to the vertical velocity perturbations found due to wave motions induced by flow over the topography. However, impacts of mountain waves on aviation go beyond the often slight, though sometimes significant, bumpiness of turbulence. Several airline accidents have been attributed to severe mountain wave induced turbulence. However, not all impacts of mountain waves on aviation are negative. Glider pilots often make use of the regions of strong upward vertical velocity to increase their altitude and fly further.

Regardless of the positive or negative impacts, improvements of our understanding of mountain waves are important for either mitigating, in the case of a negative impact, or enhancing, in the case of a positive impact, the effect. In addition, the great impacts of mountain waves on the general atmospheric circulation represent a requirement to understand mountain wave dynamics not just for their immediate small-scale impact, but also for their

influence on weather and climate on much broader scales.

As Queney et al. (1960) notes, airflow over mountains has long been known to be more irregular than that over flat terrain. In the early part of the twentieth century, driven particularly by aviation concerns, observational campaigns were conducted to better understand mountain waves. The first observations of these waves were essentially qualitative from cloud observations and glider pilot reports. While individual scientists collected and published observational results beginning in the 1930s, the first significant field campaigns were to wait until the 1950s, when the Sierra Wave Project was conducted to study wave activity generated by the Sierra Nevada mountain range in California and Nevada. The legacies of these early field campaigns have been continued in recent years by campaigns such as the Terrain-Induced Rotor Experiment (T-REX) and the DEEPly Propagating Gravity WAVE (DEEPWAVE) campaign, which was the impetus for the research presented in this manuscript.

The first theoretical studies of mountain waves came in the years within and following the Second World War. Lyra (1940) and Queney (1948) provided two-dimensional theoretical studies of a mountain in a one-layer atmosphere, i.e. where the atmosphere is isothermal and has no wind shear. While Lyra studied a rectangular mountain, Queney studied, as he referred to it in Queney et al. (1960), a "humpbacked" profile. Scorer (1949) further generalized the atmospheric structure to include two layers, and derived for the first time a solution that included a second type of mountain wave, the trapped lee wave.

Scorer (1949), as well as later studies incorporating even more atmospheric layers, such as Corby and Wallington (1956) also discovered that the trapped wave solutions were not necessarily unique. It is possible for a given atmospheric profile to support more than one trapped wave mode. These higher-order modes, while appearing as a direct result of these theoretical studies, have not previously been shown to have been either observed or appear in realistic model simulations of the atmosphere. The simulations detailed in this manuscript provide some initial indications that higher-order trapped wave modes with significant amplitude in the stratosphere can indeed be supported by realistic atmospheric structures and

generated in numerical models.

Chapter 2

BACKGROUND

In a statically stable atmospheric layer, a vertical displacement of an air parcel will tend to produce *gravity waves* (Petty, 2008), which are perhaps more properly termed *buoyancy waves* because the restoring force is buoyancy. Vertically displaced parcels will oscillate about their equilibrium point due to a difference in temperature (and therefore buoyancy) with their surroundings. A parcel displaced downward will experience an upward acceleration, while an parcel displaced upward will experience a downward acceleration. Since the vertical velocity of the parcel when it returns back to its equilibrium point is non-zero, it is again displaced and experiences another acceleration, this time in the opposite direction. This continuing cycle results in wave-like behavior.

2.1 Basic Gravity Wave Dynamics

In an inviscid and adiabatic atmosphere, the governing equations are the momentum equation,

$$\frac{D\mathbf{u}}{Dt} + 2\mathbf{\Omega} \times \mathbf{u} = -\frac{1}{\rho}\nabla p - \mathbf{g}, \tag{2.1}$$

the continuity equation,

$$\frac{1}{\rho}\frac{D\rho}{Dt} + \nabla \cdot \mathbf{u} = 0, \tag{2.2}$$

and the thermodynamic equation

$$\frac{D\theta}{Dt} = 0, \tag{2.3}$$

where $\mathbf{u}$ is the three-dimensional velocity vector, $\mathbf{\Omega}$ is the angular velocity vector of the Earth, ρ is the atmospheric density, p is the atmospheric pressure, $\mathbf{g}$ is the gravitational acceleration vector, and θ is the potential temperature (Gill, 1982). For ease of analysis,

we now assume the atmosphere is incompressible and has no variations in the meridional direction (e.g. $\partial/\partial y = 0$). Then, linearizing about a basic state $U = U(z)$, $V = 0$, $W = 0$, and $\rho_0 = \rho_0(z)$ results in the momentum equations

$$\rho_0 \left[\left(\frac{\partial}{\partial t} + U \frac{\partial}{\partial x} \right) + \frac{dU}{dz} w \right] = -\frac{\partial p'}{\partial x} \tag{2.4}$$

and

$$\rho_0 \left(\frac{\partial}{\partial t} + U \frac{\partial}{\partial x} \right) w = -\frac{\partial p'}{\partial z} - \rho' g. \tag{2.5}$$

In addition, the continuity equation becomes

$$\nabla \cdot \mathbf{u} = \frac{\partial u}{\partial x} + \frac{\partial w}{\partial z} = 0. \tag{2.6}$$

The definition of an incompressible atmosphere, that there are no changes in density following the motion of a parcel, can be expanded and linearized as follows:

$$\frac{D\rho}{Dt} = 0 \tag{2.7}$$

$$\Rightarrow \frac{\partial \rho}{\partial t} + u \frac{\partial \rho}{\partial x} + w \frac{\partial \rho}{\partial z} = 0 \tag{2.8}$$

$$\Rightarrow \frac{\partial (\rho_0 + \rho')}{\partial t} + (U + u') \frac{\partial (\rho_0 + \rho')}{\partial x} + w' \frac{\partial (\rho_0 + \rho')}{\partial z} = 0 \tag{2.9}$$

Since ρ_0 is only a function of z,

$$\frac{\partial \rho'}{\partial t} + (U + u') \frac{\partial \rho'}{\partial x} + w' \frac{\partial (\rho_0 + \rho')}{\partial z} = 0 \tag{2.10}$$

Finally, neglecting products of perturbation quantities results in

$$\frac{\partial \rho'}{\partial t} + U \frac{\partial \rho'}{\partial x} + w' \frac{d\rho_0}{dz} = 0 \tag{2.11}$$

$$\Rightarrow \left(\frac{\partial}{\partial t} + U \frac{\partial}{\partial x} \right) \rho' + \frac{d\rho_0}{dz} = 0, \tag{2.12}$$

which is Eq. 8.9.4 of Gill (1982). Following the procedure set out in Gill (1982), we can now eliminate ρ' and p' and utilize the Boussinesq approximation to obtain a single equation for w *in steady state*,

$$\frac{\partial^2 w}{\partial x^2} + \frac{\partial^2 w}{\partial z^2} + \left(\frac{N^2}{U^2} - \frac{1}{U} \frac{d^2 U}{dz^2} \right) w = 0, \tag{2.13}$$

where N is the Brunt-Väisälä frequency,

$$N = \sqrt{-\frac{g}{\rho_0}\frac{d\rho_0}{dz}}, \tag{2.14}$$

and where

$$l^2 \equiv \frac{N^2}{U^2} - \frac{1}{U}\frac{d^2U}{dz^2} \tag{2.15}$$

is termed the *Scorer parameter* [after Scorer (1949), the paper in which it was first introduced].

To review, we now have a single second-order linear homogeneous partial differential equation for vertical velocity in a two-dimensional, inviscid, adiabatic, and incompressible Boussinesq atmosphere for small motions where the Coriolis acceleration is small enough to be neglected and where the basic state wind is only a function of height.

If we assume a wave-like solution in x of the form

$$w\left(x,z\right) = \mathrm{Re}\{\hat{w}\left(z\right)e^{ikx}\}, \tag{2.16}$$

where $\hat{w}$ is a complex amplitude, e is Euler's number, i is the imaginary unit, k is the horizontal wavenumber, and $\mathrm{Re}\{f(x)\}$ denotes the real part of $f(x)$, Eq. 2.13 reduces to the second-order linear homogeneous *ordinary* differential equation

$$\frac{d^2\hat{w}}{dz^2} + \left(l^2 - k^2\right)\hat{w} = 0 \tag{2.17}$$

(Durran et al., 2015).

2.1.1 Constant N and U Atmosphere

In the case where both N and U are constant, Eq. 2.17 is an second-order linear homogeneous ordinary differential equation with constant coefficients. In this case, the general solution is

$$\hat{w}(z) = \begin{cases} c_1 e^{-mz} + c_2 e^{mz}, & k^2 > l^2 \\ c_3\cos\left(mz\right) + c_4\sin\left(mz\right), & k^2 < l^2, \end{cases} \tag{2.18}$$

where c_n are constants to be determined by the boundary conditions and $m = \left|\sqrt{l^2 - k^2}\right|$ is the vertical wavenumber. In order to ensure that the wave amplitude approaches zero as $z \to \infty$, we must choose $c_2 = 0$.

Determining the constants in the $k^2 < l^2$ case requires a little more work. First, we note that, in this case, the full solution $w(x, z)$ is

$$w(x,z) = \mathrm{Re}\{c_3 \cos(mz)\, e^{ikx} + c_4 \sin(mz)\, e^{ikx}\} \tag{2.19}$$

$$= \mathrm{Re}\{\mathrm{Re}\{(c_3 - ic_4)\, e^{imz}\} e^{ikx}\} \tag{2.20}$$

Note, however, that Eq. 2.20 is not necessarily equal to $\mathrm{Re}\{(c_3 - ic_4)\, e^{imz} e^{ikx}\}$. Therefore, it is easier to simplify the analysis by expanding Eq. 2.19 in terms of its real and imaginary components as follows:

$$\begin{aligned} w(x,z) = \mathrm{Re}\{&c_3 \cos(kx)\cos(mz) + c_4 \cos(kx)\sin(mz) \\ &+ ic_3 \sin(kx)\cos(mz) + ic_4 \sin(kx)\sin(mz)\}. \end{aligned} \tag{2.21}$$

Since $c_3, c_4 \in \mathbb{C}$, we cannot simply strike the terms containing i. However, by the product-to-sum trigonometric identities, we can rewrite Eq. 2.21 as

$$\begin{aligned} w(x,z) = &\frac{c_{3r}}{2}\left[\cos(kx - mz) + \cos(kx + mz)\right] + \frac{c_{4r}}{2}\left[\sin(kx + mz) - \sin(kx - mz)\right] \\ &- \frac{c_{3i}}{2}\left[\sin(kx + mz) + \sin(kx - mz)\right] - \frac{c_{4i}}{2}\left[\cos(kx - mz) - \cos(kx + mz)\right], \end{aligned} \tag{2.22}$$

where $c_{3r}, c_{3i}, c_{4r}, c_{4i} \in \mathbb{R} : c_3 = c_{3r} + ic_{3i}, c_4 = c_{4r} + ic_{4i}$. This result can be rearranged in terms of the sine and cosine functions:

$$\begin{aligned} w(x,z) = \frac{1}{2}[&\cos(kx + mz)\,(c_{3r} + c_{4i}) + \sin(kx + mz)\,(c_{4r} - c_{3i}) \\ &+ \cos(kx - mz)\,(c_{3r} - c_{4i}) + \sin(kx - mz)\,(-c_{4r} - c_{3i})], \end{aligned} \tag{2.23}$$

which can be expressed in complex exponential form as

$$w(x,z) = \frac{1}{2}\mathrm{Re}\{(c_3 - ic_4)\, e^{i(kx+mz)} + (c_3 + ic_4)\, e^{i(kx-mz)}\}. \tag{2.24}$$

2.1.2 Boundary Conditions

In the case where $k^2 > l^2$, the upper boundary condition was immediately apparent. The amplitude of a wave cannot become infinite as $z \to \infty$, so $c_2 = 0$. However, in the case where $k^2 > l^2$, the upper boundary condition is not as innately obvious and was in fact the cause of some debate in the mid 20th century. Several authors originally postulated that the appropriate upper boundary condition is for the phase velocity of the waves to be upward. However, a consensus eventually emerged that, since energy should be transported away from the ground, the direction of energy propagation (and hence the group velocity) should be upward, *not* the phase velocity (Queney et al., 1960; Gill, 1982).

The question then becomes, "Which choice of constants in Eq. 2.24 yields waves with upward energy propagation?" In a steady state framework, this appears to not even be a valid question, as steady-state waves must not have any net propagation of energy. If a steady-state wave were to have a net propagation of energy, that would imply the presence of an infinite source of energy, since a steady-state wave is, by definition, constant in time. Since this is obviously not physically possible, it appears impossible to determine the correct boundary condition in a solely steady state framework.

However, since steady state waves must arise as the limiting behavior of some initial time-dependent wave, we can use the group velocity of the time-dependent wave and consider the limit as it approaches steady-state (Palm and Scorer, 1958). If we do not neglect time derivatives in the step from Eq. 2.12 to Eq. 2.13, we obtain [see Gill (1982), his Eq. 8.9.7]

$$\left(\frac{\partial}{\partial t} + U\frac{\partial}{\partial x}\right)^2 \left(\frac{\partial^2}{\partial x^2} + \frac{\partial^2}{\partial z^2}\right) w + N^2 \frac{\partial^2 w}{\partial x^2} - \frac{d^2 U}{dz^2}\left(\frac{\partial}{\partial t} + U\frac{\partial}{\partial x}\right)\frac{\partial w}{\partial x} = 0. \tag{2.25}$$

Substituting in a wavelike solution in x and z, $w(x,z) = \mathrm{Re}\{e^{i(kx+nz-\omega t)}\}$, where $n = \pm m$ can be of either sign and $k, m, \omega \geq 0$, we obtain

$$-k^2\omega^2 - n^2\omega^2 + U^2k^4 + U^2k^2n^2 - N^2k^2 - \frac{d^2U}{dz^2}\left(-k\omega - k^2\right) = 0. \tag{2.26}$$

In the constant N and U case, the term involving a second derivative of U is zero, and so

the equation reduces to

$$\omega^2 = U^2k^2 - \frac{N^2k^2}{k^2+n^2}. \tag{2.27}$$

Since $U, N, k, \omega \geq 0$,

$$\Rightarrow \omega = Uk \pm \frac{Nk}{\sqrt{k^2+n^2}}. \tag{2.28}$$

However, for steady state waves, $\omega = 0$. Only the negative root can yield $\omega = 0$, so we disregard the positive root. Then, the vertical group velocity is

$$c_{gz} = \frac{\partial\omega}{\partial n} = \frac{knN}{(k^2+n^2)^{\frac{3}{2}}}. \tag{2.29}$$

It follows that, in order for the vertical group velocity to be positive (i.e. energy to propagate upward), $\text{sgn}(k) = \text{sgn}(n)$.

Note that the original assumption was for a wave-like solution of the form $w(x,z) = \text{Re}\{e^{i(kx+nz-\omega t)}\}$. Returning to our original equation (Eq. 2.24), we see that the only solution supporting upward energy propagation is the $e^{i(kx+mz)}$ term, since in this case, $n = m$.

It may appear that this result is dependent on the particular assumed solution. However, if we assumed a wavelike solution of the form $w(x,z) = \text{Re}\{e^{i(kx-nz-\omega t)}\}$, we would have obtained that $\text{sgn}(k) = -\text{sgn}(n)$. Then, in this case, $n = -m$, and therefore, $w(x,z) = \text{Re}\{e^{i(kx-(-m)z-\omega t)}\} = \text{Re}\{e^{i(kx+mz-\omega t)}\}$, so the solution supporting upward energy propagation is again the $e^{i(kx+mz)}$ term.

Now, returning to Eq. 2.24, we have shown that $c_3 + ic_4 = 0$, and therefore

$$w(x,z) = \frac{1}{2}\text{Re}\{(c_3 - ic_4)\, e^{i(kx+mz)}\}. \tag{2.30}$$

All that remains is to determine the value of $c_3 - ic_4$. Luckily, we still have one more boundary condition to apply. Since air cannot flow into or out of the surface, the flow at the surface must be tangential to the topography (Gill, 1982).

The simplest terrain profile to analyze mathematically is a series of sinusoidal ridges of the form $h(x) = \text{Re}\{h_0 e^{ikx}\}$, where h_0 is a complex terrain height $h_0 = h_{0r} + ih_{0i}$, where $h_0 r$ is the height of the cosine contribution to the terrain and $h_0 i$ is the height of the sine

contribution to the terrain. At the lower boundary, we we require that the velocity normal to the terrain be identically zero (i.e. no air flows into or out of the surface). We can approximate this boundary condition as [see Durran (1990), his Eq. 4.18]

$$w(x,0) = u_0 \frac{\partial h}{\partial x}, \tag{2.31}$$

which in this case becomes

$$w(x,0) = U \frac{\partial \left[h_0 e^{ikx} \right]}{\partial x} = Uikh_0 e^{ikx}. \tag{2.32}$$

Then, it follows that $\frac{1}{2}(c_3 - ic_4) = Uikh_0$, and

$$w(x,z) = \mathrm{Re}\{Uikh_0 e^{i(kx+mz)}\}. \tag{2.33}$$

In addition, returning to the first part of Eq. 2.18, we apply the same boundary condition to yield $w(x,z) = \mathrm{Re}\{Uikh_0 e^{ikx-mz}\}$. Therefore, to summarize,

$$w(x,z) = \begin{cases} \mathrm{Re}\{Uikh_0 e^{ikx-mz}\}, & k^2 > l^2 \\ \mathrm{Re}\{Uikh_0 e^{i(kx+mz)}\}, & k^2 < l^2, \end{cases} \tag{2.34}$$

with $m = \left|\sqrt{l^2 - k^2}\right|$.

2.1.3 Generalization to Arbitrary Terrain Profiles

While the previous result is useful for understanding the basic dynamics of mountain waves, it is nonetheless too idealized for most purposes. Since there is no physical place with an infinite series of sinusoidal ridges, the next logical step is to generalize the lower boundary condition to take into account different terrain profiles. However, since any subdomain of an arbitrary function can be represented as an infinite series of sines or cosines, the above result is not as trivial as it may appear. In fact, since the above equation is linear, the solution to a mountain wave problem with an arbitrary terrain profile is simply the sum of the solutions for each component in its Fourier series.

2.1.4 Wave Trapping

In a multiple-layer atmosphere where the Scorer parameter (Eq. 2.15) decreases with height, it is possible for wave trapping (also known as wave ducting, for example in Markowski and Richardson (2010)) to occur. Trapped waves are resonant waves generated by the interaction of a wave with its reflection. The interaction of the primary wave, which is upward propagating, and its reflection, which is downward propagating, results in a wave in the lower layer that extends downstream of the ridge and has no tilt (Durran, 1990).

A necessary condition for the presence of trapped waves in a two-layer atmosphere was derived by Scorer (1949):

$$l_L^2 - l_U^2 \geq \frac{\pi^2}{4H^2}, \tag{2.35}$$

where l_L and l_U are the Scorer parameters of the lower and upper layers, respectively, and H is the depth of the lower layer. This necessary criteron derives from employing matching conditions to the individual solutions for the upper and lower layers. For resonant waves to occur, the upper layer must have evanescent waves, i.e. $k^2 > l_U^2$ and the lower level must have propagating waves, i.e. $k^2 < l_L^2$. Then, applying a kinematic matching condition, where vertical velocity is constant across the interface, and a dynamic matching condition, where pressure is constant across the interface, results in

$$\cos(mH) + \frac{\mu}{m}\sin(mH) = 0 \tag{2.36}$$

$$\cot(mH) = -\frac{\mu}{m}, \tag{2.37}$$

where $m = (l_L^2 - k^2)^{1/2}$ and $\mu = (k^2 - l_U^2)^{1/2}$. Since μ and m are always positive between l_U and l_L, the cotangent function must be negative on some portion of this interval for a resonant mode to be possible. The cotangent function monotonically decreases as its argument increases (except at its singularities). Therefore, since $l_U < k$, $(l_L^2 - k^2)^{1/2} H < (l_L^2 - l_U^2)^{1/2} H$, and therefore, $\cot\left[(l_L^2 - l_U^2)^{1/2} H\right] < \cot\left[(l_L^2 - k^2)^{1/2} H\right]$ (where there are no singularities). Since we require $\cot\left[(l_L^2 - k^2)^{1/2} H\right] \leq 0$, it follows that a necessary condition

is

$$\cot\left[\left(l_L^2 - l_U^2\right)^{1/2} H\right] < 0. \tag{2.38}$$

The smallest value for which Eq. 2.38 is true is $\pi/2$, and therefore this reduces to Scorer (1949)'s criterion (Eq. 2.35). However, the cotangent function is periodic, and there will therefore be infinitely many regions where $\cot\left[\left(l_L - l_U\right)^{1/2} H\right] < 0$. These regions occur when $\frac{(2n-1)\pi}{2} < \theta < n\pi$, for $n = 0, 1, 2, ...$ Then, the number of resonant modes increases every time $\left(l_L - l_U\right)^{1/2} H$ surpasses an odd multiple of $\pi/2$. In particular, a given two layer structure will support exactly n modes when

$$\left[\frac{(2n-1)\,\pi}{2H}\right]^2 \leq l_L^2 - l_U^2 \leq \left[\frac{(2n+1)\,\pi}{2H}\right]^2 \tag{2.39}$$

(Queney et al., 1960). Therefore, as long as there is a substantial difference between the Scorer parameters of the two layers, higher order trapped wave modes are possible.

2.1.5 Stratospheric Waves

Danielsen and Bleck (1970) provide the only reference to trapped waves in the stratosphere known to the author. While their solutions do contain trapped wave modes in the stratosphere, their Scorer parameter profiles decay exponentially and asymptotically approach zero with height. Therefore, it is not surprising that their wave solutions would result in trapped waves in the stratosphere.

Indeed, much of the current literature on gravity wave activity in the stratosphere refers to one of two mechanisms: either wave propagation from below, such as discussed in Smith et al. (2008) or Jiang et al. (2012), or secondary wave generation resulting from wave breaking, which is discussed in Vadas et al. (2003). Besides the aforementioned Danielsen and Bleck (1970), no studies are known to the author to discuss the possibility of trapped waves in the stratosphere. All of the solutions obtained in Durran et al. (2015) with a stratosphere feature leaky modes. The results shown in this manuscript are therefore potentially some of the first to show the possible existence of trapped waves with significant amplitude in the stratosphere.

2.2 DEEPWAVE

The DEEPly Propagating Gravity WAVE (DEEPWAVE) experiment was a field campaign conducted over New Zealand during the austral winter of 2014. The purpose of DEEPWAVE was to study gravity waves and their interactions with the broader atmosphere as they propagate from the surface all the way to the mesosphere and lower thermosphere (Fritts et al., 2015). To this end, the DEEPWAVE campaign utilized substantial instrumentation, including aircraft and ground based instrumentation. In addition, observations were supplemented with high resolution models.

While the purpose of DEEPWAVE was to study propagating waves, the wealth of data collected from the instrumentation and modeling infrastructure is valuable for studying other types of waves as well, including trapped waves. The primary observation period lasted from 29 May 2014 to 27 July 2014. However, immediately after the end of the primary observation period, a strong event occurred.

2.2.1 28 July 2014 Case

Figure 2.1 shows the general orientation of the topography of New Zealand in relation to major cities and sounding locations. In particular, Hokitika is located on the west coast of the South Island, upstream of the Southern Alps. During DEEPWAVE, Hokitika hosted an Instrument Sounding System (ISS) which provided both wind profiler and radiosonde data. A time series of profiler data from Hokitika on 28 Jul 2014 is shown in Fig. 2.2. In the temporal vicinity of 12 UTC, strong northwesterly winds over 20 m/s are present at 2500 m AGL. The wind profiler was located at an elevation of 69 m. The highest peak in the Southern Alps is Aoraki/Mt. Cook, at an elevation of 3724 m, and there are a large number of peaks in the Southern Alps with elevations of over 2500 m. Therefore, the strong northwesterly winds at 2500 m are directly impinging on a large portion of the topography of the South Island. With the wind direction being essentially normal to the topography, this lower-level wind profile is favorable for the generation of mountain waves.

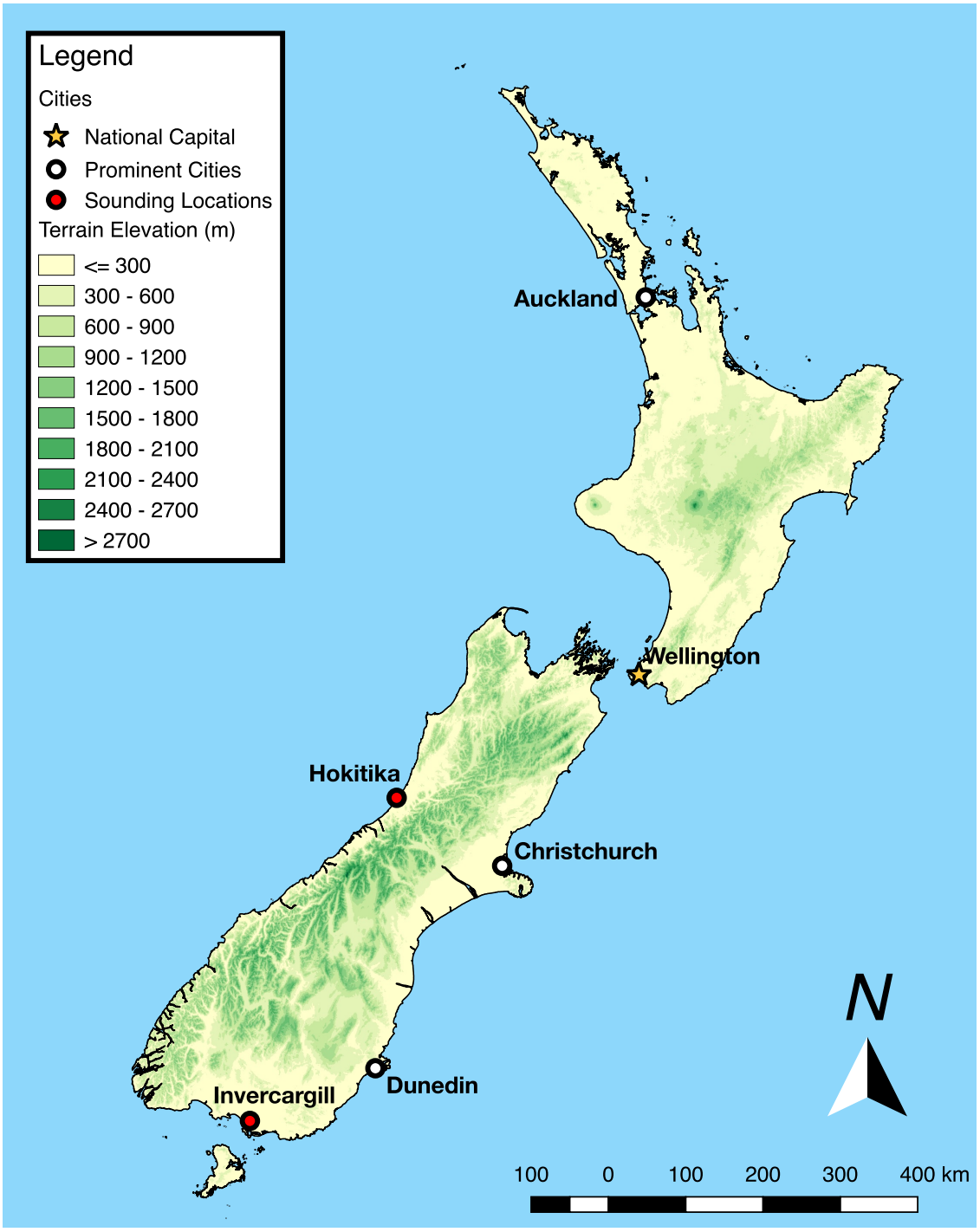

Figure 2.1: Map of New Zealand including major cities and terrain profile. Locations of DEEPWAVE soundings are marked in red.

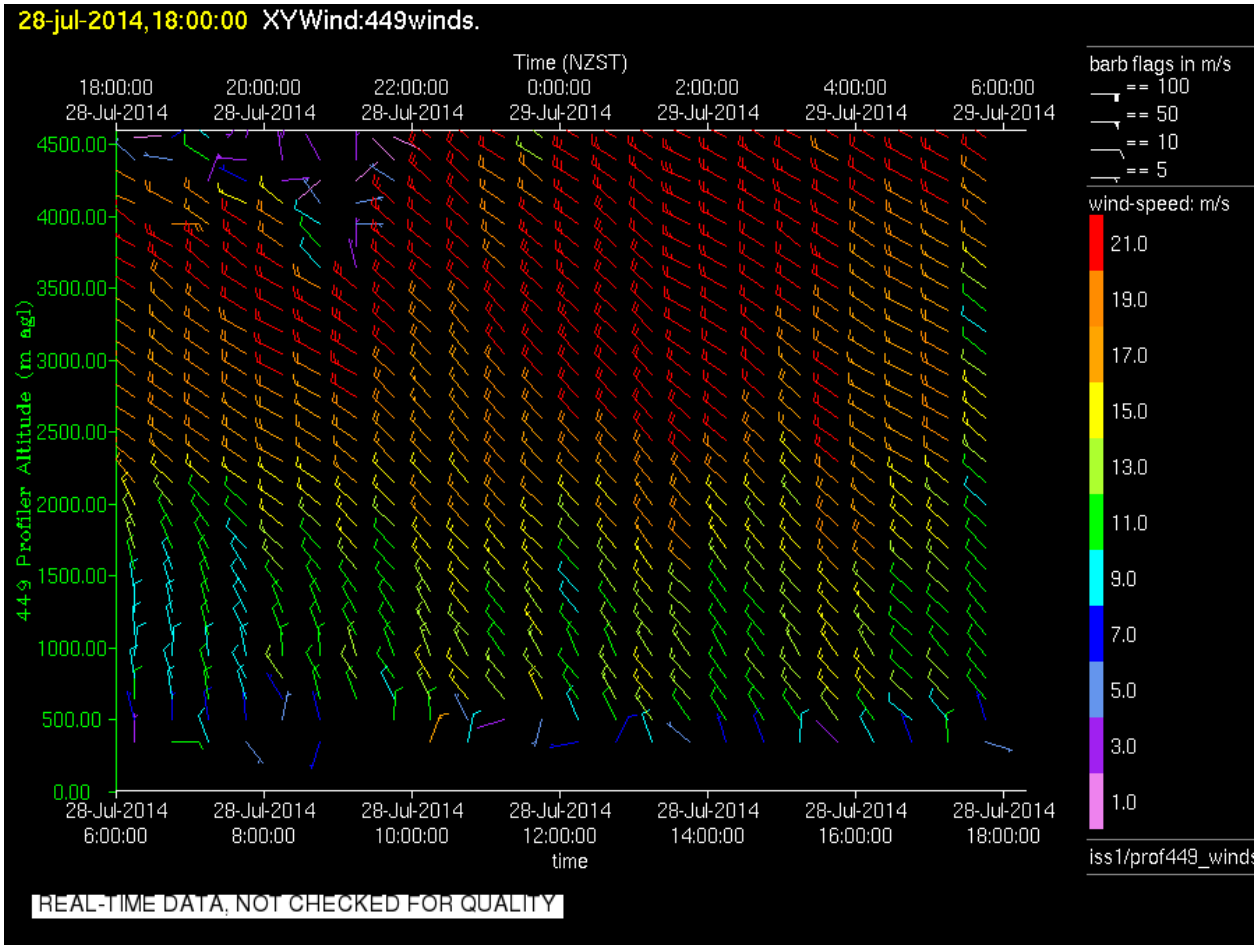

Figure 2.2: Time series of wind profiler data from Hokitika from 06 UTC 28 July 2014 to 18 UTC 28 July 2014. Times are denoted in New Zealand Standard Time (NZST, UTC+12) on top and UTC on the bottom.

The upper level wind profile is revealed by an 11 UTC 28 July 2014 sounding from Hokitika (Fig. 2.3). The wind is approximately northwesterly from about 1 to 11 km, but above 11 km, there is a layer of counterclockwise directional shear such that the winds approach westerly by about 12 km. Above this level, the winds remain approximately directionally constant up to the top of the plotted sounding at 100 hPa (16 km). In addition, the wind is quite strong in this region (over 60 knots at about 15 km), which, as was shown in Section 2.1.4, has significant implications for wave trapping.

Figure 2.3 also reveals moist and approximately saturated conditions from the surface up to approximately 7 km. Saturation has been demonstrated to change the effective Brunt-Väisälä frequency, and hence the Scorer parameter and the structure of the trapped lee waves, in these regions (Durran and Klemp, 1982). However, the theoretical components of the present study do not consider moisture effects. While these effects may indeed be significant, it is worthwhile to determine to what extent dry dynamics can explain the observed phenomena. Hokitika is located on the upstream side of the topography, and therefore, much of the moisture may be removed on the upstream side by orographic processes. Regardless, investigating and quantifying the effects of moisture on these waves remains an important aspect of future work.

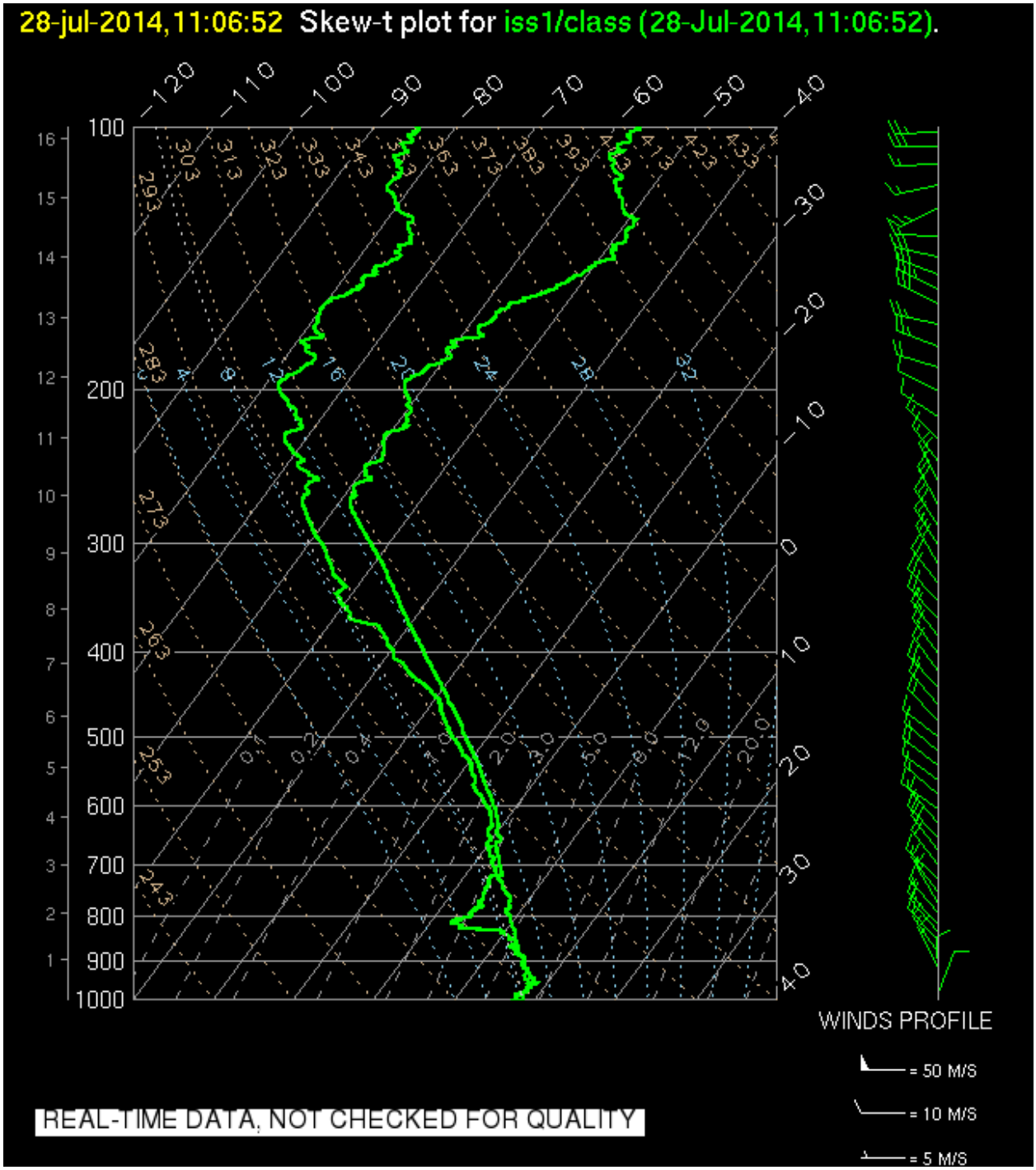

Figure 2.3: Skew-T Log-p diagram from Hokitika at 11 UTC 28 July 2014. There is directional shear in the profile such that the winds rotate from the northwesterly to westerly above approximately 11 km.

Chapter 3

3D SIMULATION METHODOLOGY

The stratospheric waves were investigated using three-dimensional WRF simulations. These simulations varied in both atmospheric structure and terrain. There were two different atmospheric structures: the fully evolving (FE) flow, derived from GFS analysis, and the horizontally homogenous (HH) steady flow, which was derived from the fully evolving flow as described in Section 3.2. There were three different terrain profiles: the full terrain (FT), based off of the actual terrain of New Zealand; the "no lee" terrain (NL), based off of the terrain of New Zealand but with side ridges off of the main crest removed; and the idealized terrain (IT), consisting of one large Witch of Agnesi ridge with smaller side ridges. All six combinations of atmospheric structure and terrain were run.

3.1 WRF Model Description

All simulations were conducted with version 3.8.1 of the Weather Research and Forecasting - Advanced Research WRF (WRF-ARW) model (Skamarock et al., 2008). The parameterizations used in the FE simulations were Thompson microphysics, YSU boundary layer physics, Kain-Fritsch cumulus (for the 18 km resolution domain only), Dudhia shortwave radiation, RRTM longwave radiation, Monin-Obhukov surface layer physics, and the Noah land-surface model. The HH runs did not utilize any parameterizations and were run with purely dry dynamics and no Coriolis force. In addition, a free-slip surface was utilized in the HH runs, so the terrain profiles were reduced to half-height to compensate for the increased wave amplitude due to the lack of friction.

A Rayleigh damping layer was also imposed in the upper 8 km (for FE runs) or 10 km (for HH runs) of the model domain. This layer utilized a profile for the damping coefficient as

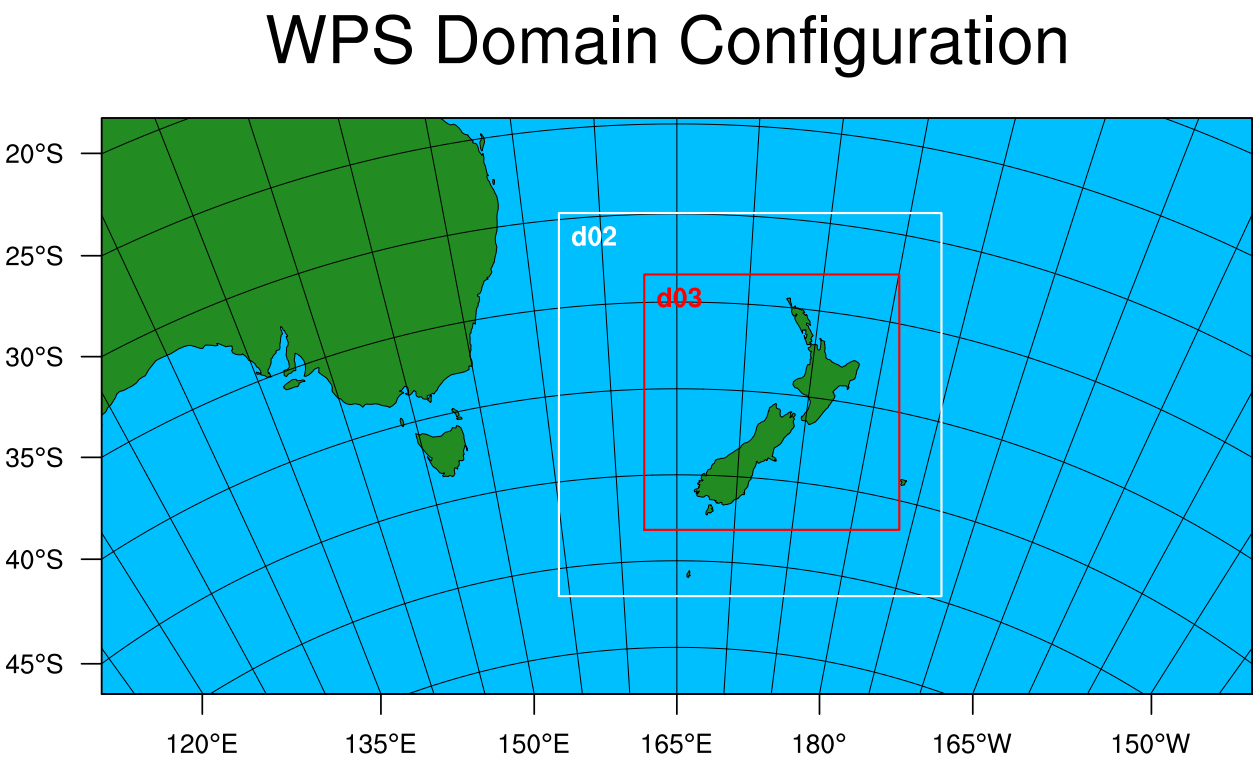

Figure 3.1: Domains for the FE simulations. The resolution of the domains are 18 km, 6 km, and 2 km, respectively.

discussed in Durran (1981). This particular profile provides a significant amount of damping while still minimizing wave reflection off of the bottom of the damping layer.

3.1.1 Domain Configuration

The domain configuration for the FE runs is shown in Fig. 3.1. The domains consisted of three nests at 18 km, 6 km, and 2 km horizontal resolution, respectively. The horizontal domain used a Lambert conformal conic map projection, with its standard longitude defined to be 165°E and its true latitudes to be 30°S and 60°S. The outermost domain is centered on the point 41°S 165°E, and is 400 grid points west to east and 200 grid points north to south. The first inner domain is 400 by 400 grid points with its lower left corner located at the point

$(160, 35)$ of the outer domain. The innermost domain is 799 by 799 grid points and has its lower left corner located at the point $(90, 70)$ of the first inner domain. The domain has 109 vertical levels, with an approximate model top of 10 hPa, which is located at approximately 30 km. The model time step was 45, 15, and 5 seconds from the outermost domain to the innermost.

The HH domain was 798 by 798 grid points in the horizontal with a 1 km grid spacing. The model has 135 vertical levels with a model top at 30 km. The model time step was 5 seconds.

3.2 Terrain Configuration

3.2.1 Realistic Terrain

Full Terrain (FT)

The FT simulations used terrain from the United States Geological Survey (USGS) GMTED2010 dataset at 30-arc-second resolution. This terrain was interpolated to the WRF model grid by the WRF Preprocessing System (WPS) in its standard manner. The resulting terrain grids were then filtered to damp the shortest resolvable (and therefore most unstable) wavelength, the $2\Delta x$ wavelength. This was accomplished using a nine-point two-dimensional Laplacian stencil, such that

$$h_{i,j} = h_{i,j} + a \left[\text{sum} \left(\begin{bmatrix} \frac{1}{6} & \frac{2}{3} & \frac{1}{6} \\ \frac{2}{3} & -\frac{10}{3} & \frac{2}{3} \\ \frac{1}{6} & \frac{2}{3} & \frac{1}{6} \end{bmatrix} \circ \begin{bmatrix} h_{i-1,j+1} & h_{i,j+1} & h_{i+1,j+1} \\ h_{i-1,j} & h_{i,j} & h_{i+1,j} \\ h_{i-1,j-1} & h_{i,j-1} & h_{i+1,j-1} \end{bmatrix} \right) \right], \tag{3.1}$$

where a is a coefficient chosen such that the $2\Delta x$ wave is maximally damped, $\circ$ denotes the Hadamard, or Schur, product (element-by-element multiplication), and "sum" represents the sum of all elements in the matrix.

"No Lee Ridges" Terrain (NL)

In order to determine to what extent ridges off the main crest of the Southern Alps generate these waves, a second profile was developed and run with these ridges removed. To do this, a normalized Witch of Agnesi curve was used to create a multiplier for the terrain. The maximum of the curve was positioned on a line along the crest of the Southern Alps, which was defined by placing the origin at the point (300 km, 250 km) and defining the slope of the line to be 35° (Fig. 3.2). The terrain was left unmodified to the north and west of this line but was tapered off to the south and east by using a normalized Witch of Agnesi curve as a multiplicative factor (Fig. 3.3). This factor was defined as follows:

$$M(x,y) = \begin{cases} 1, & x,y \in \text{upstream} \\ \frac{8a^3}{y^2+4a^2} / \max_{x,y}\left(\frac{8a^3}{y^2+4a^2}\right), & x,y \in \text{transition zone} \\ 0, & x,y \in \text{downstream}, \end{cases} \tag{3.2}$$

where $a = 5$ grid points (10 km). The resulting terrain profile is shown in Fig. 3.4.

3.2.2 Idealized Terrain (IT)

This simulation introduced, for the first time, a fully idealized terrain profile. This served two purposes. First, demonstrating that an idealized ridge can force the trapped wave modes simplifies the analysis because the important factor is then not the irregularity of the terrain. Second, since the idealized profile is much more regular, it should produce more coherent and consistent waves.

The idealized ridge utilized in this simulation consisted of one main ridge, oriented from southwest to northeast in the same manner as the Southern Alps. In addition, smaller side ridges extruded southward from the main ridge to represent small scale ridges and valleys found in the Southern Alps. All of the ridges followed a $\cos^4(x)$ terrain profile on their edges,

$$h(x) = \frac{h_0}{16}\left[1 + \cos^4\left(\frac{\pi x}{4a}\right)\right], \tag{3.3}$$

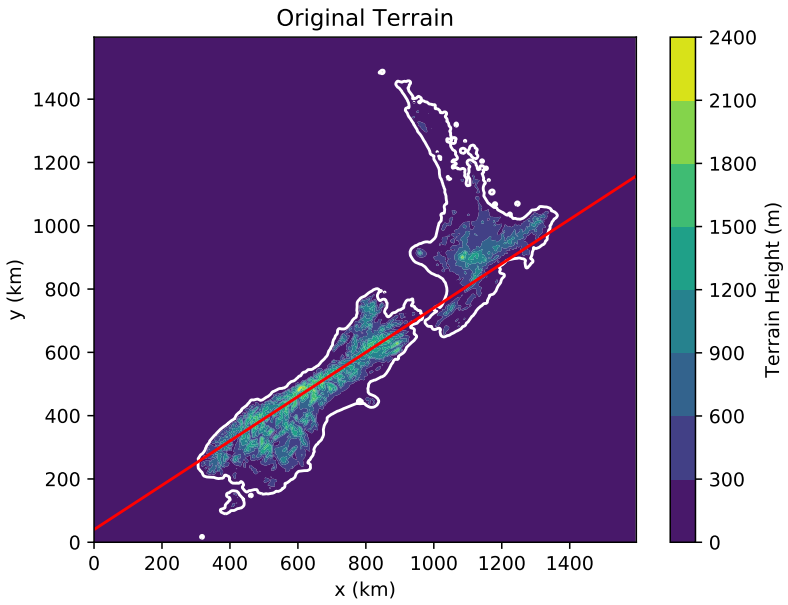

Figure 3.2: Realistic terrain profile of New Zealand. The line defining the maximum for the Witch of Agnesi curve used to generate the NL terrain is shown in red.

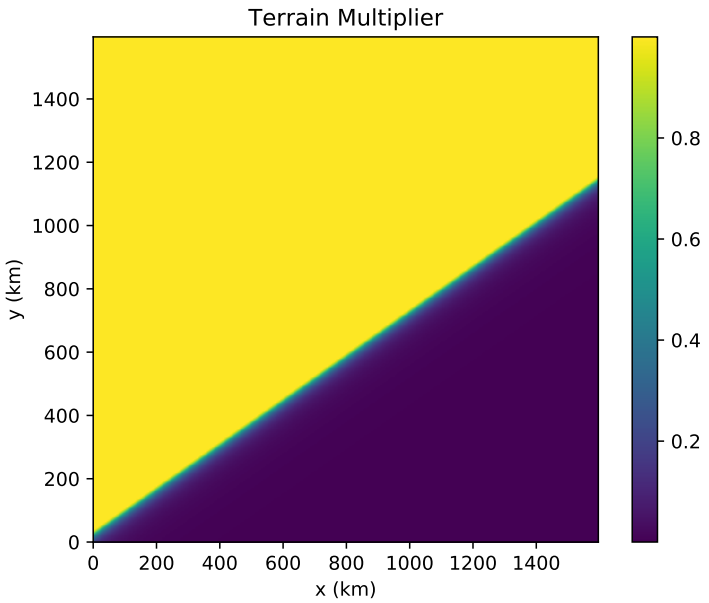

Figure 3.3: Multiplicative factor used to generate the NL terrain profile.

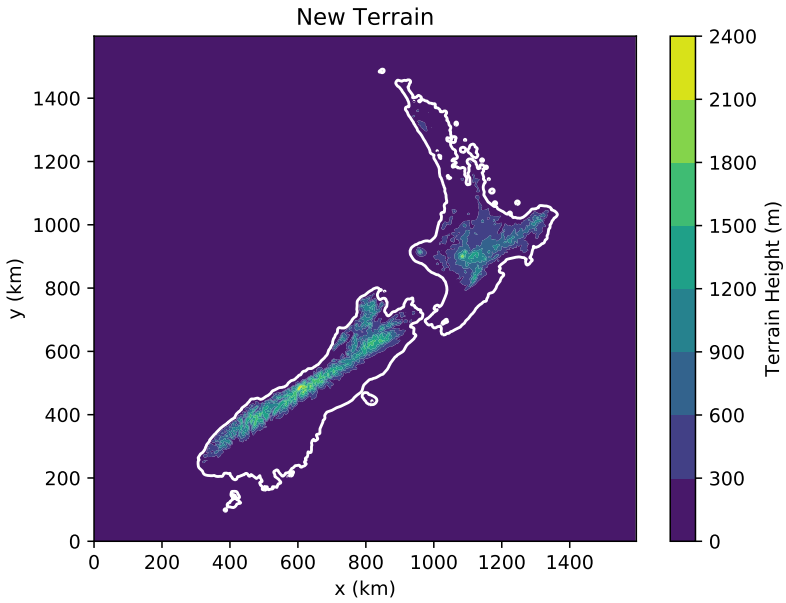

Figure 3.4: Resulting NL terrain profile.

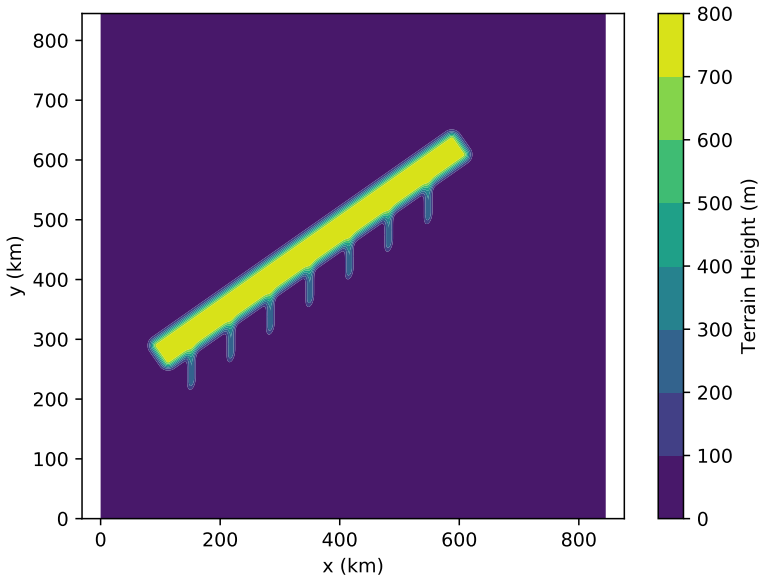

Figure 3.5: Idealized terrain profile used for the IT runs.

where h_0 is the maximum mountain height and a is the half-width of the mountain. The side ridges followed this profile throughout, but the main ridge incorporated a flat "plateau" at the top, which was 15 km wide and 300 km long. The maximum mountain height of the main ridge was 750 m, and the maximum height of the side ridges was 300 m. The half-width of the main ridge was 10 km, while the half-width of the side ridges was 5.5 km. The side ridges were 66 km apart.

This choice of idealized ridge is designed to effectively generate both the cross-mountain waves (generated by the main ridge) and the transverse waves (more effectively forced by the side ridges). The distance between the side ridges, 66 km, was chosen to be a multiple of a wavelength of 11 km. This wavelength was approximately that of the waves generated in the FENL simulation (see section 4.1.2).

3.3 Atmospheric Structure

3.3.1 Fully Evolving Flow (FE)

The FE runs were initialized using the National Centers for Environmental Prediction (NCEP) Global Forecast System (GFS) analyses at 00 UTC 27 July 2014 and run for 48 hours, with boundary conditions provided by additional GFS analyses every three hours. The outermost domain was first run for six hours of spin-up time, and then the inner two domains began integration using initial and boundary conditions from the outer domain. Two-way communication between nests was enabled, so all domains were allowed to influence each other.

3.3.2 Steady, Horizontally Homogeneous Flow (HH)

The horizontally homogeneous sounding was generated from the wind field of the FENL simulation at the time of the strongest extent of the waves (after 31 hours of integration of the innermost domain, corresponding to 13 UTC 28 July 2014). First, a background zonal and meridional wind were derived by low-pass filtering the total wind fields with a wavelength cutoff of 200 km. This cutoff was chosen as the shortest wavelength that resulted in a qualitatively "smooth" background field. Then, a line was drawn parallel to and just upstream of the Southern Alps, and a cross section of the flow along that line was taken. The line was defined as the line passing through the point $(150, 175)$ at an angle of $35°$ above the horizontal. This cross section was then extended northwest and southeast to the boundaries (Fig. 3.7). A thermodynamic profile was specified corresponding to a piecewise Brunt-Väisälä frequency profile (Fig. 3.9), which was subjectively derived from the cross-section. The boundary conditions were then fixed, and the flow was integrated to steady state without terrain present (Fig. 3.8) to achieve a balanced wind field. The steady state flow was than averaged horizontally in a box upstream of the location corresponding to the South Island, with the lower-left corner at $(50, 0)$ and the upper-right corner at $(550, 500)$.

The resulting wind profile is shown in Fig. 3.10, plotted as zonal and meridional compo-

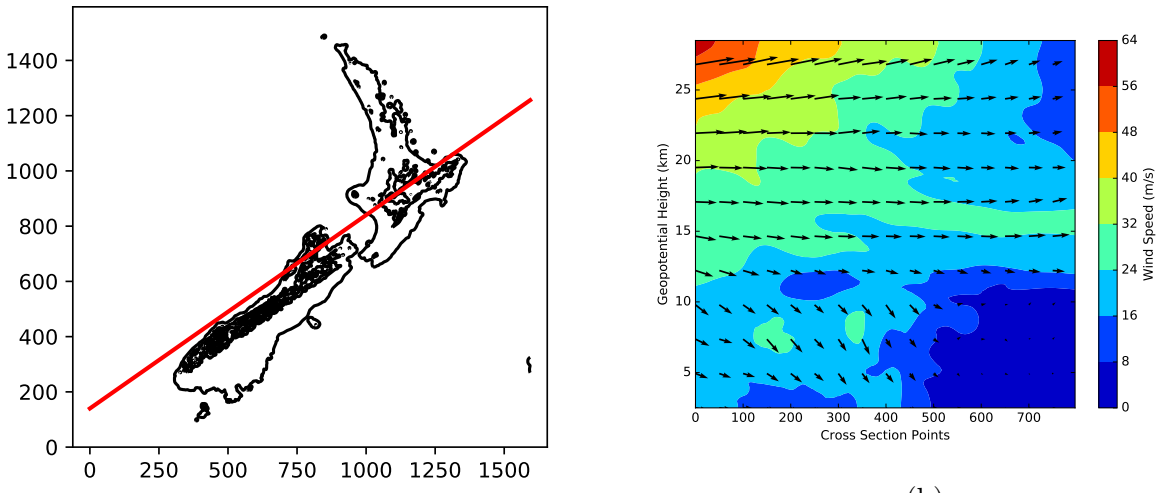

(a)

(b)

Figure 3.6: Cross section used to initialize the run to determine the HH sounding. The cross section was taken at along the line marked in (3.6a), and is shown in (3.6b). The vectors shown represent the horizontal wind.

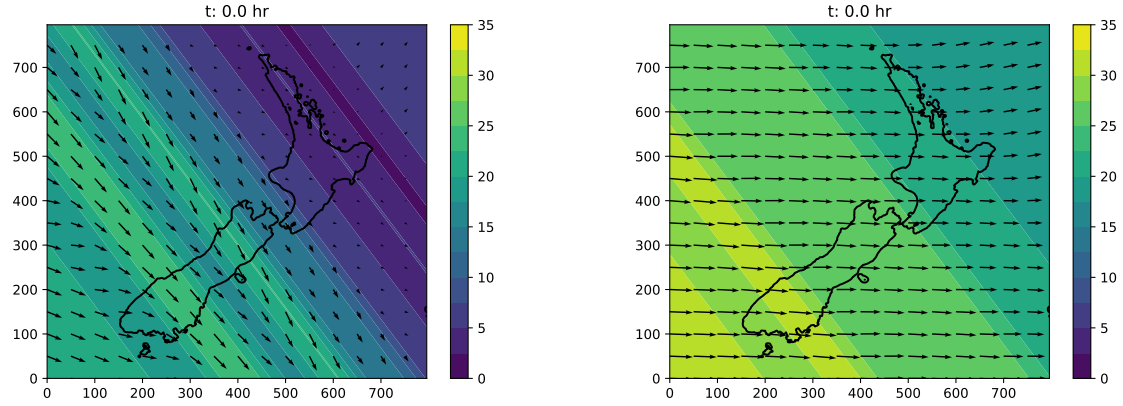

(a) z=3 km

(b) z=15 km

Figure 3.7: Initial conditions for horizontal velocity at two levels for the simulation used to generate the HH sounding. Filled contours represent the magnitude of the horizontal wind. The outline of New Zealand is for reference only; the actual simulation did not incorporate terrain.

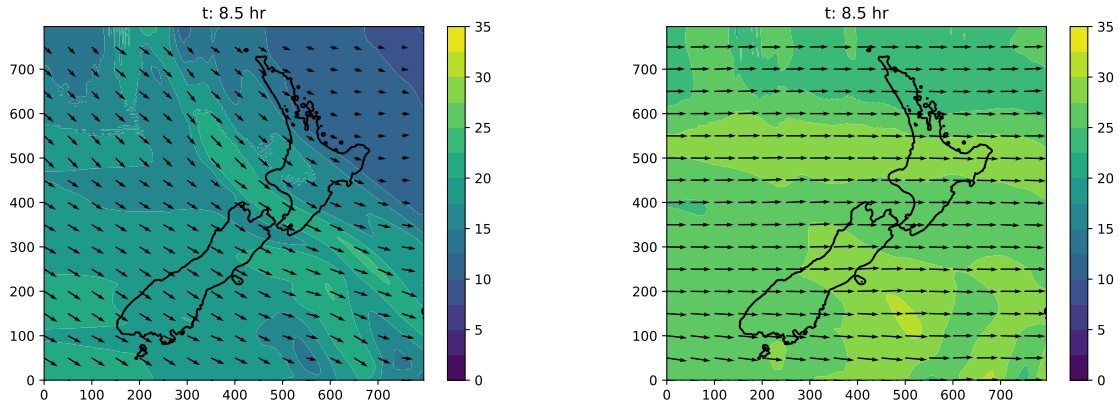

(a) z=3 km

(b) z=15 km

Figure 3.8: Horizontal velocity fields at two levels after 8.5 hours of integration to achieve a balanced flow. Filled contours represent the magnitude of the horizontal wind. The HH sounding was derived by averaging over a box with its lower-left corner at (50, 0) and its upper-right corner at (550, 500).

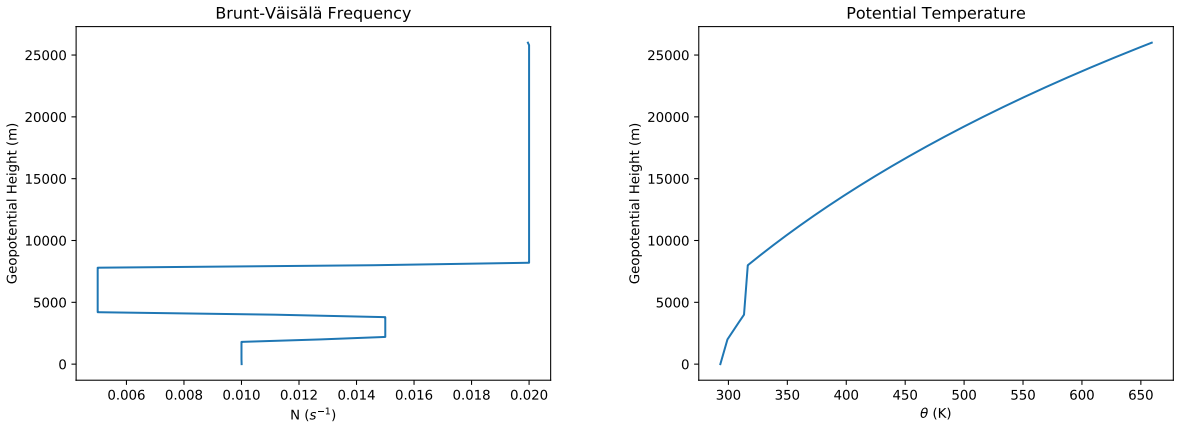

(a) Brunt-Väisälä Frequency (N)

(b) Potential Temperature (θ)

Figure 3.9: Input thermodynamic structure for the HH runs. The potential temperature is derived from the specified Brunt-Väisälä frequency field.

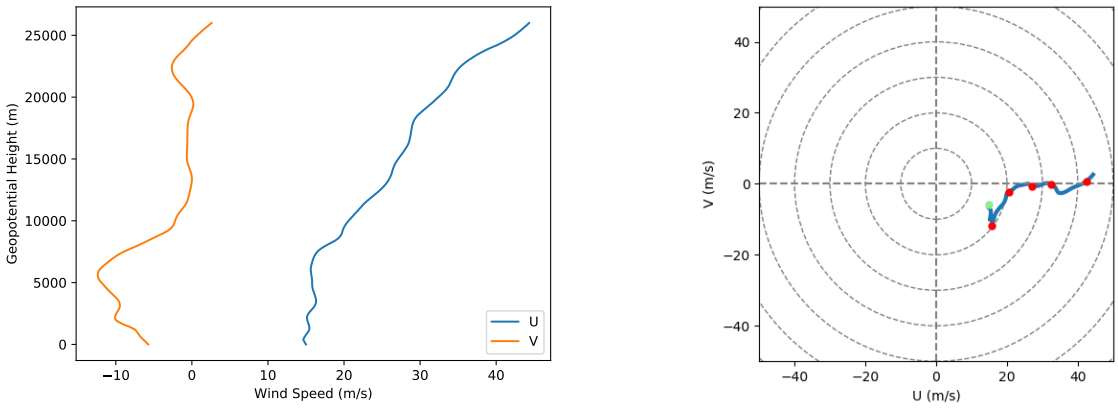

(a) (b)

Figure 3.10: Input wind profile to the HH simulations, visualized as both wind components (3.10a) and as a hodograph (3.10b). The dots in the hodograph are located every 5000 m, with the green dot located at the surface.

nents (Fig. 3.10a) and as a hodograph (Fig. 3.10b). This profile has a couple of significant features. The wind is almost perfectly perpendicular to the main crest of the Southern Alps at the surface and in the lower troposphere. This is an ideal situation for mountain wave forcing. However, there is directional shear with height such that above 10 km, the wind is nearly zonal. The wind magnitude also increases above 10 km, reaching a maximum of over 40 m/s at 25 km. Since the Brunt-Väisälä frequency is constant at these altitudes (Fig. 3.9a), the first term in the Scorer parameter will decrease with height above 10 km. The first term usually dominates, so this is a favorable wind profile for wave trapping in the stratosphere. Indeed, Figure 3.11 reveals that the Scorer parameter computed using the total magnitude of the wind decreases with height above approximately 12 km. However, this computation does not take into account the directionality of the wind, a distinction which will become important in Chapter 5.

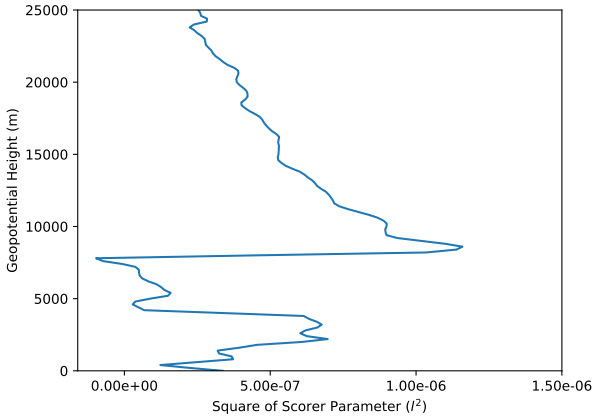

Figure 3.11: Vertical profile of the Scorer parameter (l^2) derived from the thermodynamic profiles in Fig. 3.9 and the total magnitude of the wind profile in Fig. 3.10.

3.4 Model Runs

All six combinations of terrain and atmospheric structure were simulated, and the individual model runs are denoted by four letter abbreviations. The first two letters denote the atmospheric structure as defined above: FE, for fully-evolving, and HH, for horizontally-homogeneous. The last two letters denote the terrain configuration, also as defined above: FT, for the most realistic terrain; NL, for the terrain with the lee-side ridges removed; and

		Atmospheric Structure	
		Fully Evolving	Idealized Horizontally Homogeneous
Terrain	Full Terrain	FEFT	HHFT
	No Lee Ridges	FENL	HHNL
	Idealized	FEIT	HHIT

Table 3.1: Summary of model run abbreviations.

IT, for the completely idealized terrain. Table 3.1 summarizes the abbreviations for the six runs that are used in the rest of the manuscript.

Chapter 4
3D SIMULATION RESULTS

4.1 FE Simulations

4.1.1 FEFT Simulation

Vertical velocity from the FEFT simulation is shown in Fig. 4.1. The behavior in the lower troposphere (Fig. 4.1a) is characteristic of a classic trapped wave pattern, with waves oriented parallel to the main mountain ridge and extending downstream. However, the behavior further aloft is quite distinct. The lower tropospheric waves decay with height, as expected, but a second wave regime begins to appear. At 11 km (Fig. 4.1b), the trapped waves in the lower troposphere have mostly disappeared (although some remnants remain), while the second regime is not yet apparent. This level therefore represents a minimum in the wave amplitude. Further aloft, the second wave regime becomes much more apparent, as can be seen at 15 km altitude (Fig. 4.1c).

In contrast to the classic trapped wave in the lower troposphere, the waves in the upper troposphere and lower stratosphere (UTLS) region exhibit some distinctly interesting properties. Even though the main axis of the Southern Alps are oriented from southwest to northeast, these waves appear to be mostly oriented from south to north. In addition, since the waves do not appear to be present throughout most of the troposphere, at first glance it may appear that they are not directly coupled to the topography. However, further simulations (see below) refute this and indeed demonstrate a direct coupling between this wave mode and the topography.

A vertical cross section from west to east through these waves (Fig. 4.2) reveals a relatively complex picture. In the lower and mid troposphere (below 8 km) the waves appear to be oriented vertically, which is typical of trapped waves. In addition, over the small ridge

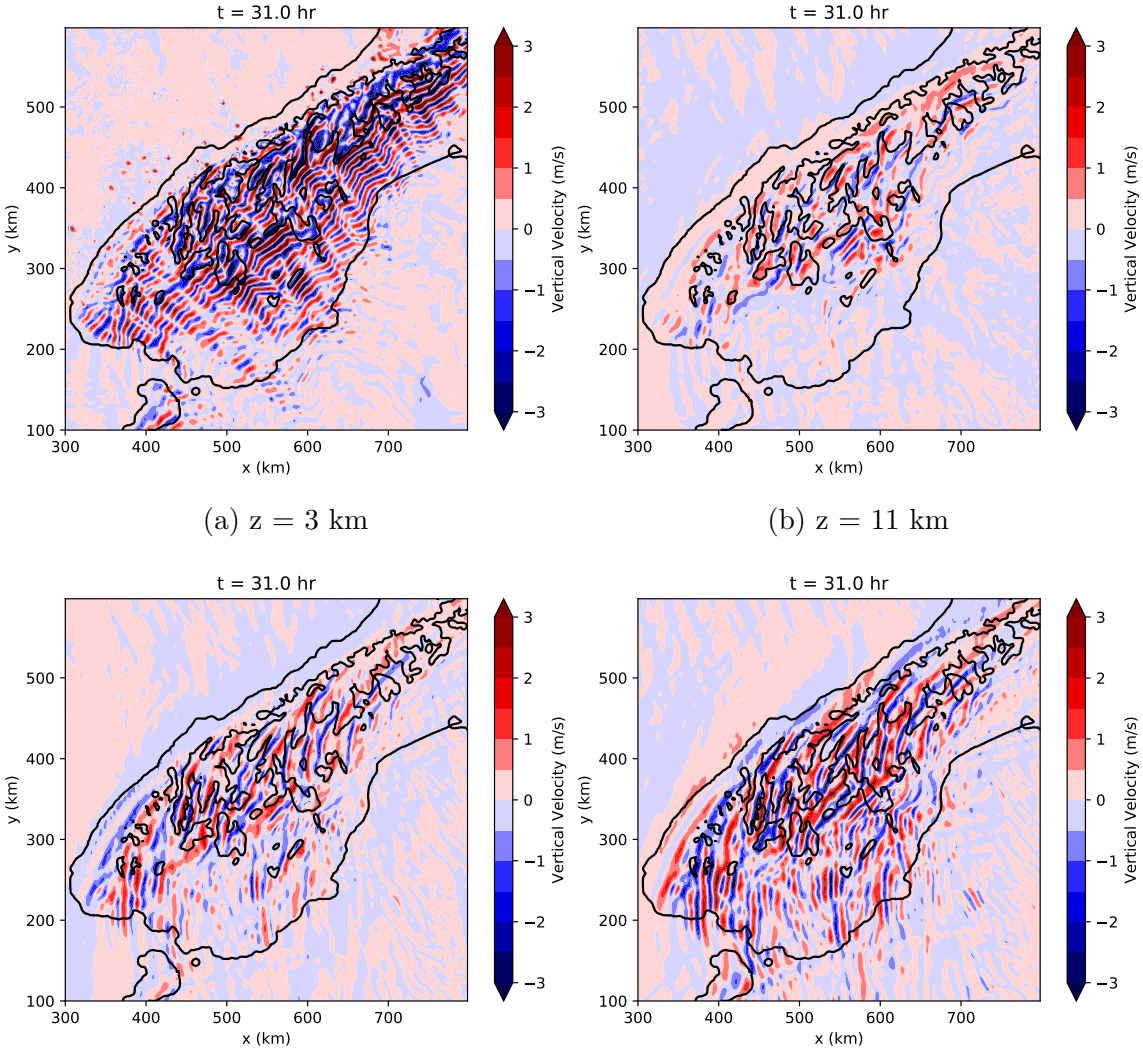

(a) z = 3 km

(b) z = 11 km

(c) z = 15 km

(d) z = 20 km

Figure 4.1: Vertical velocity at various heights in the troposphere and lower stratosphere at hour 31 of the FEFT simulation.

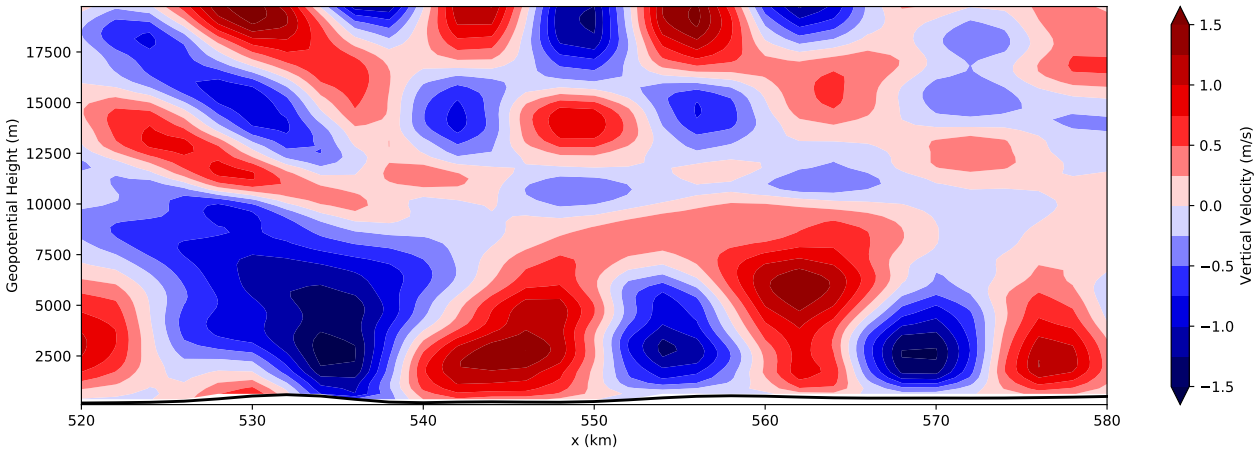

Figure 4.2: Vertical cross-section of vertical velocity of the FEFT run located at $y = 240$ km at $t = 31$ hr.

in the topography from 520 to 540 km, the vertical velocity maxima slope upstream with height. This is a signature of propagating waves and is expected above a mountain crest. However, immediately downstream of the propagating waves (from 540 to 570 km) and above 10 km, there exist waves whose maxima are again vertically oriented. In addition, there are regions of positive vertical velocity directly above regions of negative vertical velocity, and vice versa, with a zero at approximately 16 km. This is perhaps indicative of a higher order trapped wave mode in the stratosphere.

4.1.2 FENL Simulation

The NL topography results in a much clearer picture of the waves (Fig. 4.3). The lower level trapped waves are much more regular and are clearly oriented along the ridge (Fig. 4.3a), and the minimum at 11 km is much more apparent, with only some small wave amplitude at the downstream edge of the topography (Fig. 4.3b). The north-south oriented waves are also more regular and more discernible. In addition, a potential first indication of a coupling to the topography is present, as the northern extent of the wave maxima appear to be potentially associated with the downstream edge of the topography in Fig. 4.3c.

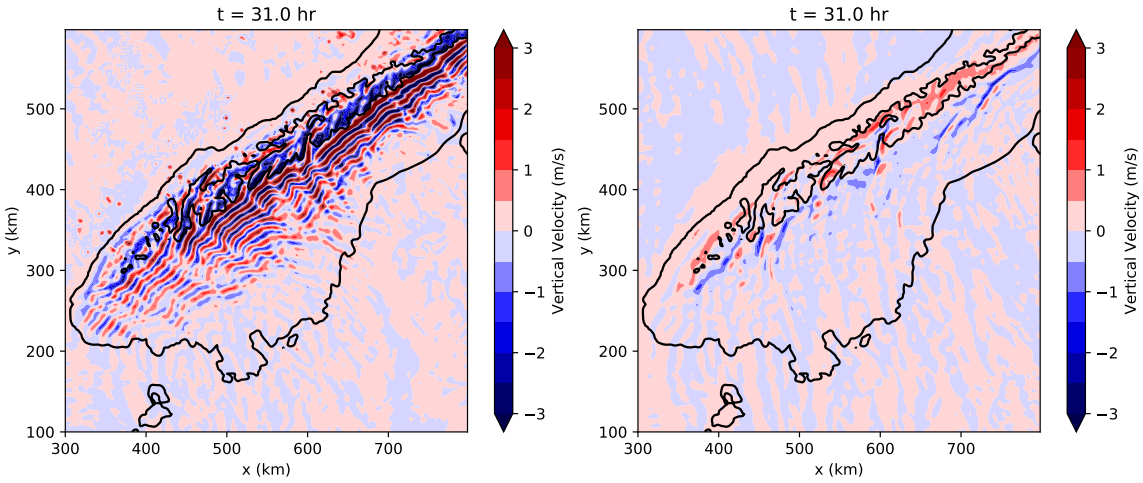

(a) z = 3 km

(b) z = 11 km

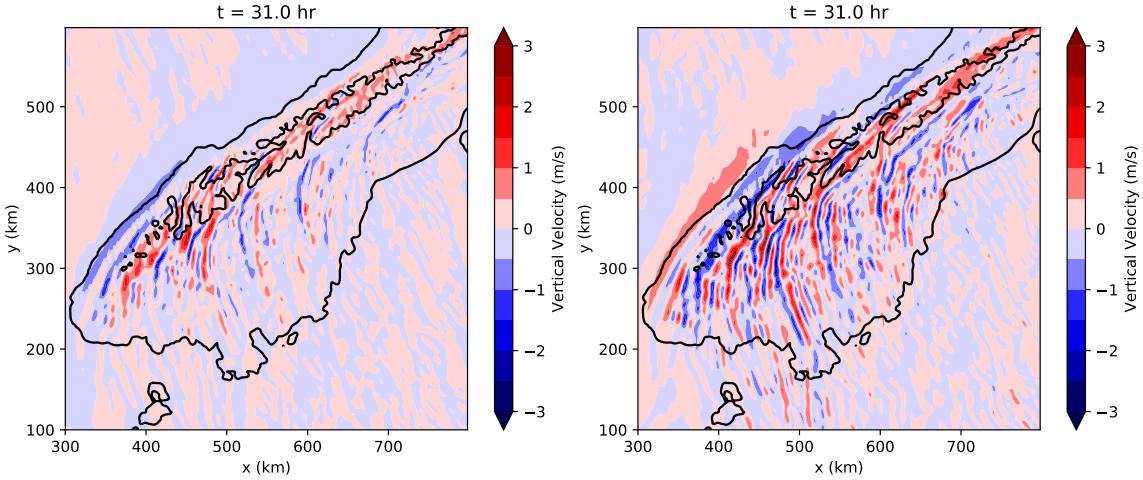

(c) z = 15 km

(d) z = 20 km

Figure 4.3: As in Fig. 4.1, but for the FENL simulation.

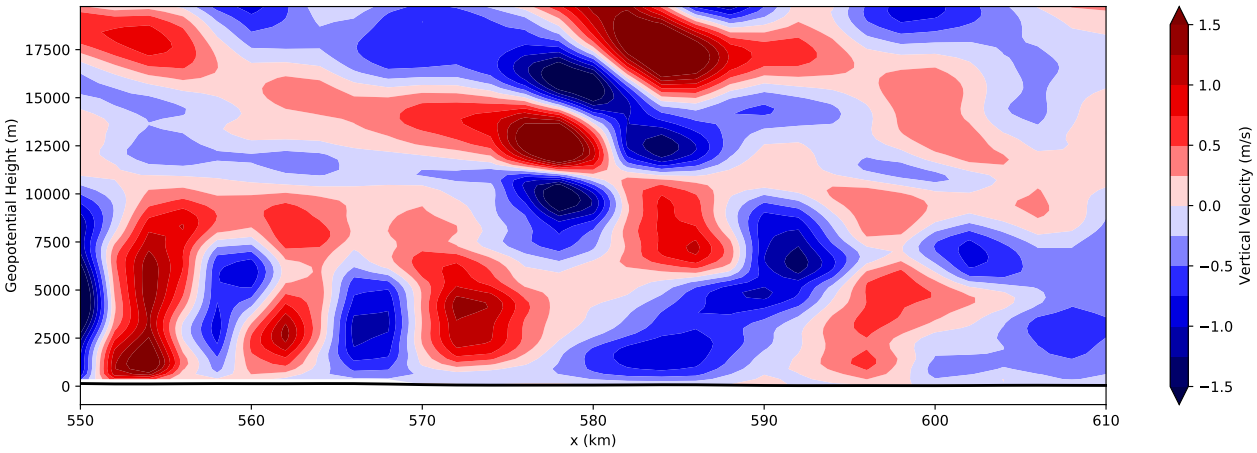

Figure 4.4: As in 4.2, but for the FENL run at $y = 380$ km and $t = 32$ hr.

A west-east vertical cross section (Fig. 4.4) shows a strong indication of a trapped wave mode in the stratosphere, with nodal lines located at approximately 11 km and 14.5 kilometers. However, there is perhaps some indication of wave propagation as well, as there is some upstream tilt to the maxima, especially above the second nodal line at 14.5 km. This would be consistent with the signature of a leaking wave mode, which has a region of vertical propagation above the trapped portion of the wave. A leaking wave mode may also explain the lack of more than one wavelength downstream, as the upward leakage of wave energy could lead to strong downstream decay.

4.1.3 FEIT Simulation

The idealized terrain of the FEIT simulation generates the north-south waves as well, which have a maximum at approximately 17 km. In addition, the FEIT simulation produces strong cross-mountain trapped waves in the lower troposphere, which are consistent with those generated by the realistic topographies. A vertical cross section (Fig. 4.6) reveals a potential higher order mode, which is most evident from $x = 300$ km to $x = 320$ km. There appear to be at least two nodal lines located at approximately $z = 11$ km and $z = 15$ km.

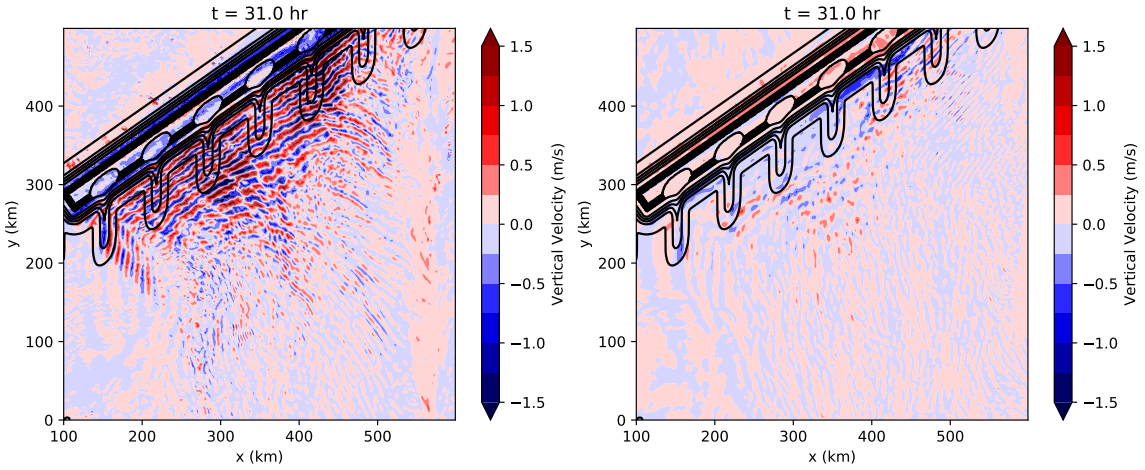

(a) z = 3 km

(b) z = 11 km

(c) z = 15 km

(d) z = 20 km

Figure 4.5: As in Fig. 4.1, but for the FEIT simulation.

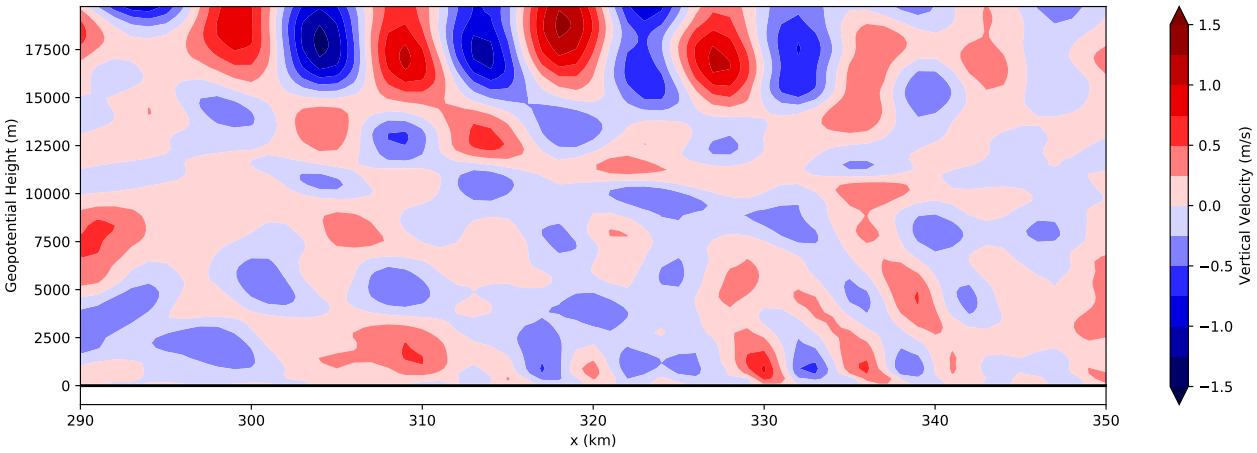

Figure 4.6: As in Fig. 4.2, but for the FEIT run at $y = 221$ km and $t = 31$ hr.

4.2 HH Simulations

4.2.1 HHFT Simulation

Figures 4.7 and 4.8 show the HHFT simulation after 5 and 10 hours of integration, respectively. At 3 km, there are robust cross-mountain waves at 5 hours. These waves at still present after 10 hours, but there is much more wave interaction and also apparent wave breaking in the middle of the ridge. This region of wave breaking corresponds to the location of the highest peaks in the Southern Alps. Above a minimum in wave amplitude at 11 km (Figs. 4.7b and 4.8b), robust south-north waves are apparent at 15 km (Figs. 4.7c and 4.8c). However, at 20 km (Figs. 4.7d and 4.8d), the orientation of the waves is closer to southwest-northeast, similar to that of the cross-mountain waves in lower levels. A west-east vertical cross-section (Fig. 4.9) shows what appears to be a higher-order mode with two nodal lines at approximately 7 and 11 km. This mode is much more robust than those in the FE simulations, and has a signal across at least five wavelengths.

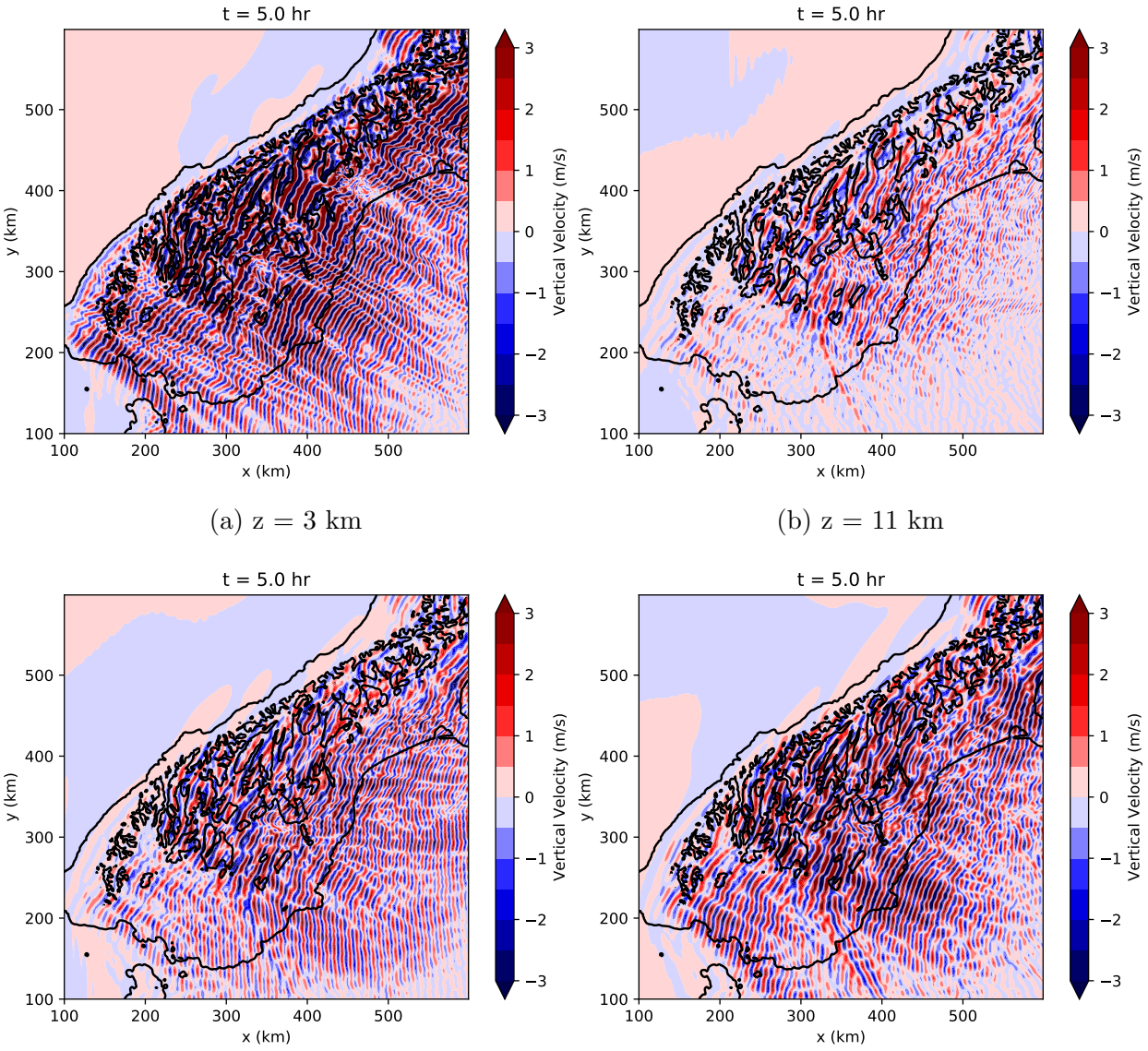

(a) z = 3 km

(b) z = 11 km

(c) z = 15 km

(d) z = 20 km

Figure 4.7: Vertical velocity at hour 5 of the HHFT run.

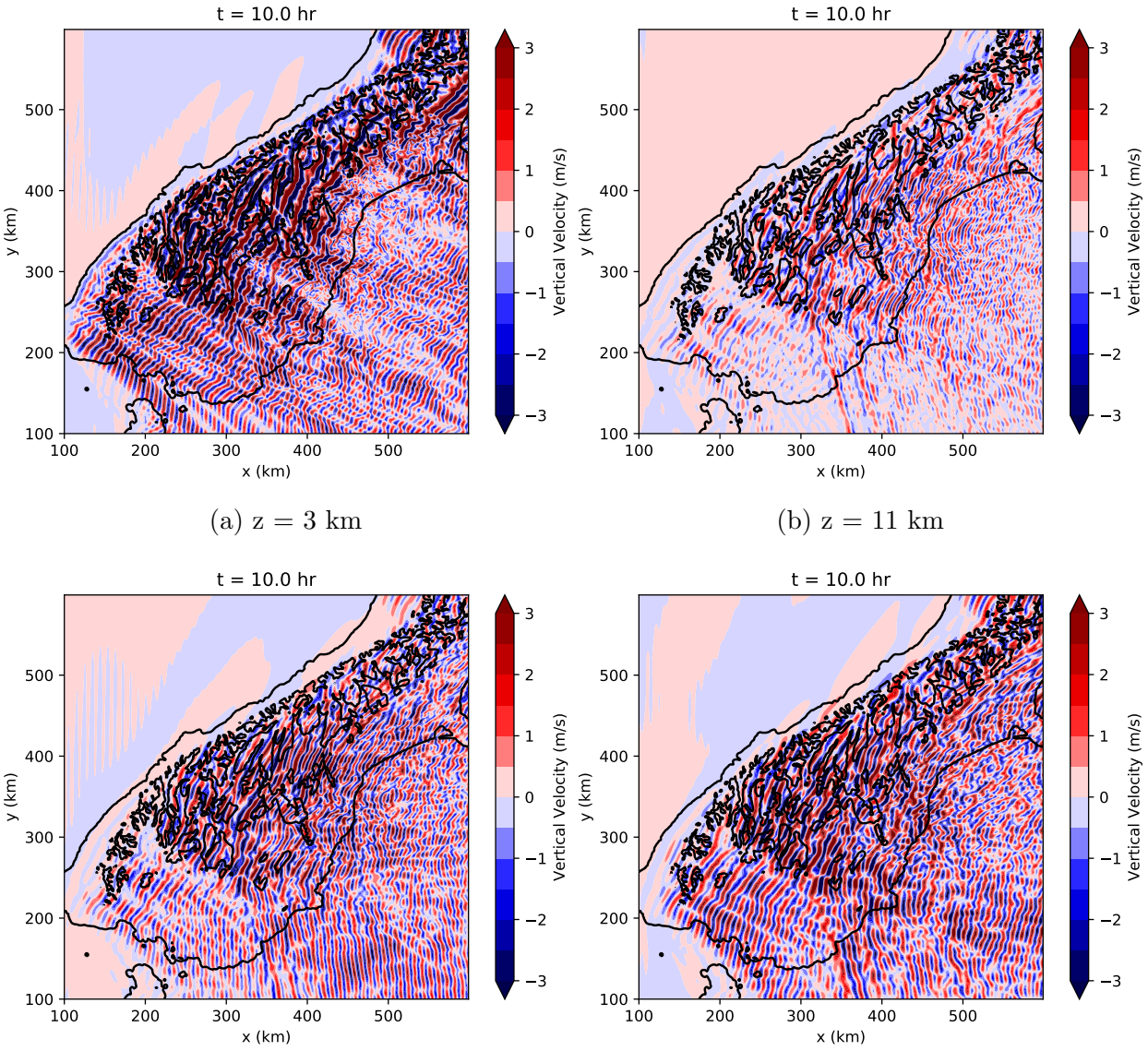

(a) z = 3 km

(b) z = 11 km

(c) z = 15 km

(d) z = 20 km

Figure 4.8: As in Fig. 4.10, but for hour 10.

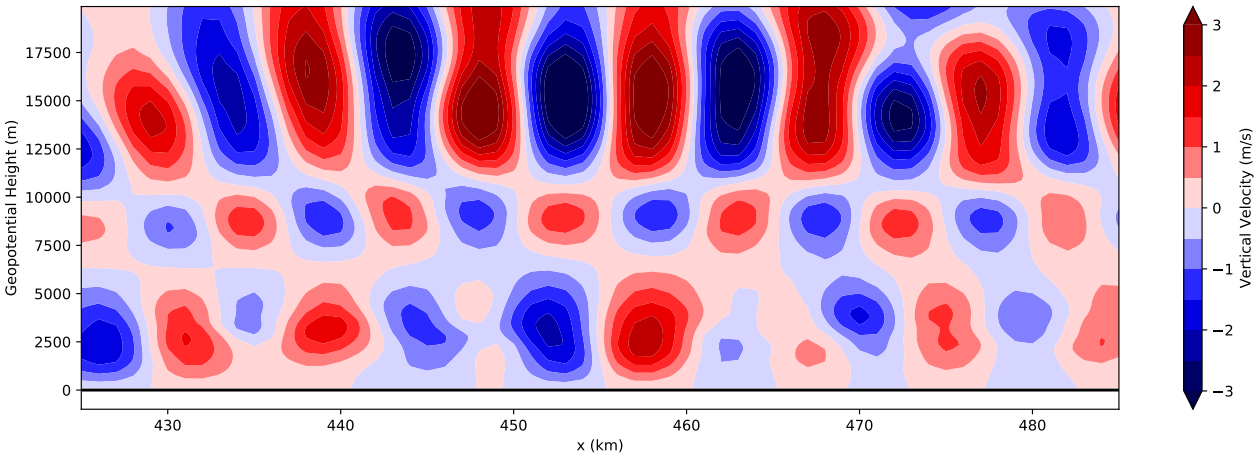

Figure 4.9: As in Fig. 4.2, but for the HHFT run at $y = 134$ km and $t = 10$ hr.

4.2.2 HHNL Simulation

The HHNL simulation demonstrates similar wave patterns as the HHFT simulation, but it also reveals interesting wave behavior in the lower troposphere. Figures 4.10 and 4.11 show vertical velocity after 5 and 10 hours of integration, respectively. The lower tropospheric cross mountain trapped waves are again present at 3 km and decay up to 11 km. In addition, the south-north waves are apparent above this level, where they appear to increase in amplitude with height until 20 km.

However, this simulation, particularly at five hours of integration time, also appears to show the south-north waves in certain areas in the lower troposphere (Fig. 4.10a). It therefore appears possible that the south-north waves are indeed present in the lower troposphere, but that the wave response is largely dominated by the cross mountain waves in this region. This is then potentially a superposition of two wave modes, one with a maximum in the lower troposphere and another with a maximum in the stratosphere. The west-east vertical cross-section (Fig. 4.12) again reveals a higher-order mode with two nodal lines at 7 km and 11 km. This is also a robust mode, with at least five wavelengths present. While the middle and upper maxima are consistently coupled, the lower layer exhibits different behavior. The

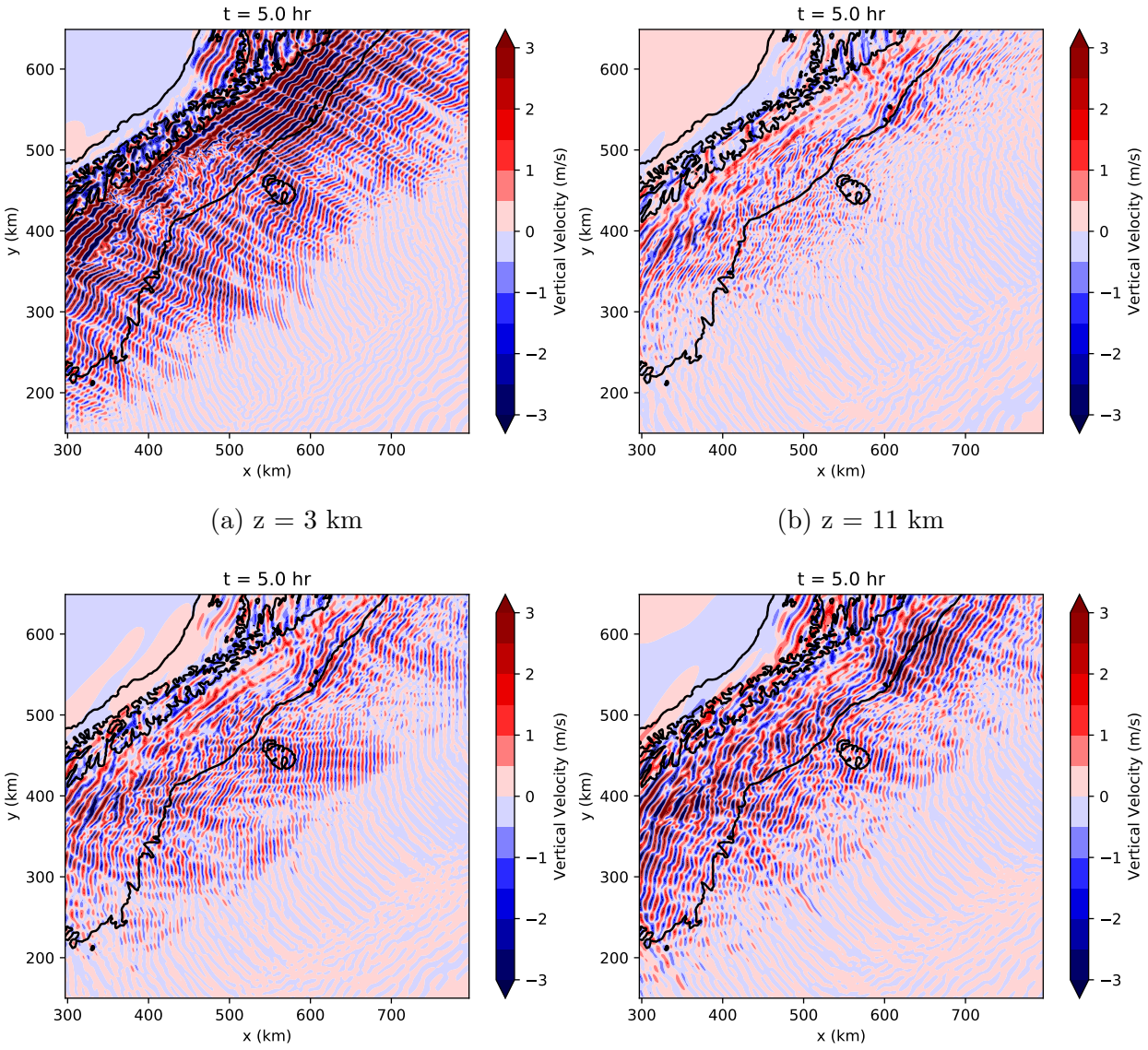

(a) z = 3 km

(b) z = 11 km

(c) z = 15 km

(d) z = 20 km

Figure 4.10: Vertical velocity at hour 5 of the HHNL run.

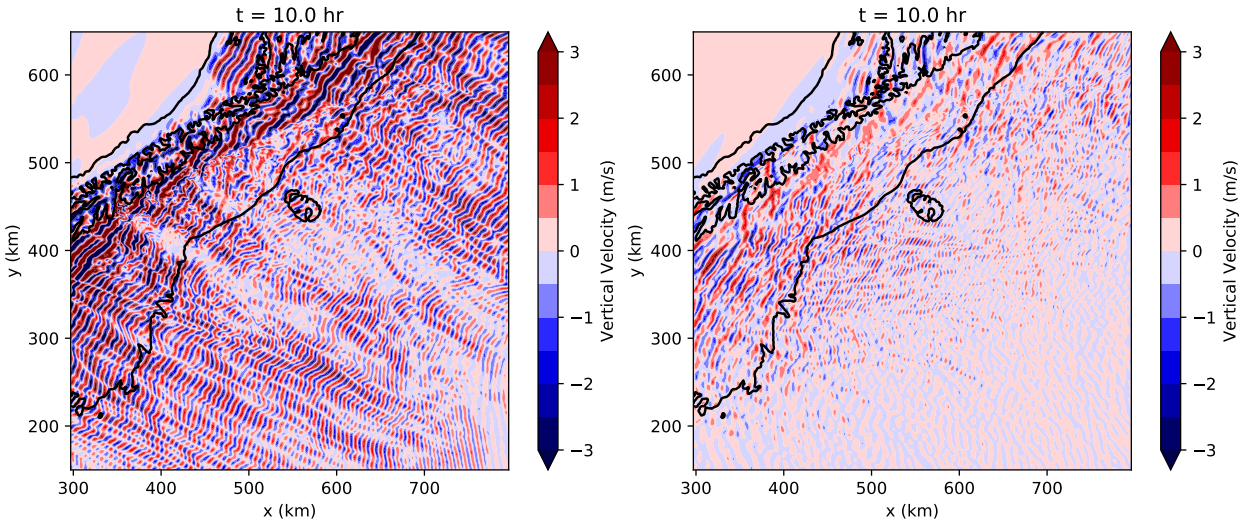

(a) z = 3 km

(b) z = 11 km

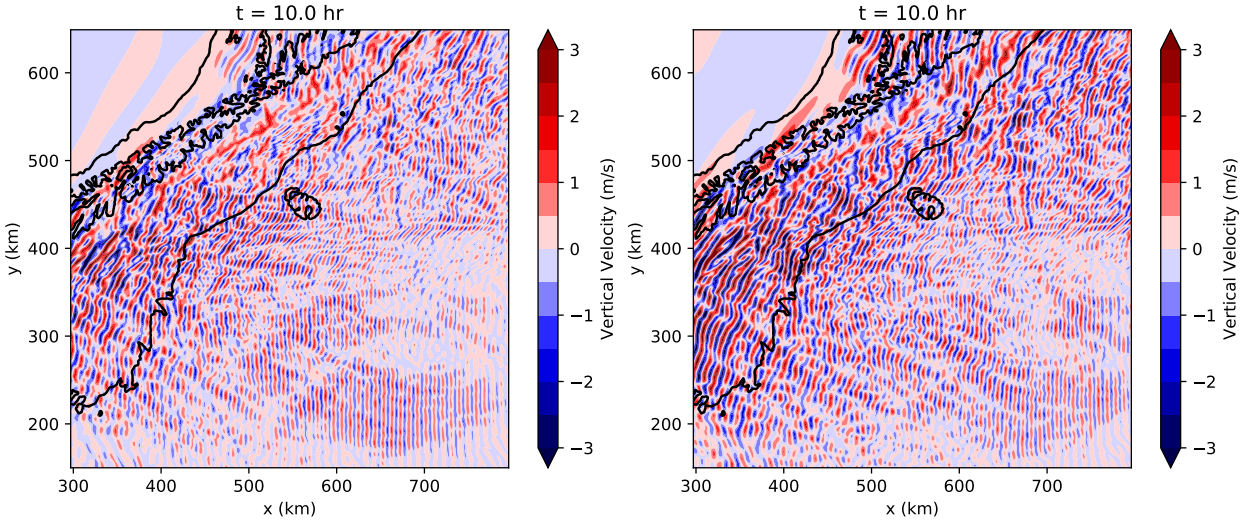

(c) z = 15 km

(d) z = 20 km

Figure 4.11: As in Fig. 4.10, but for hour 10.

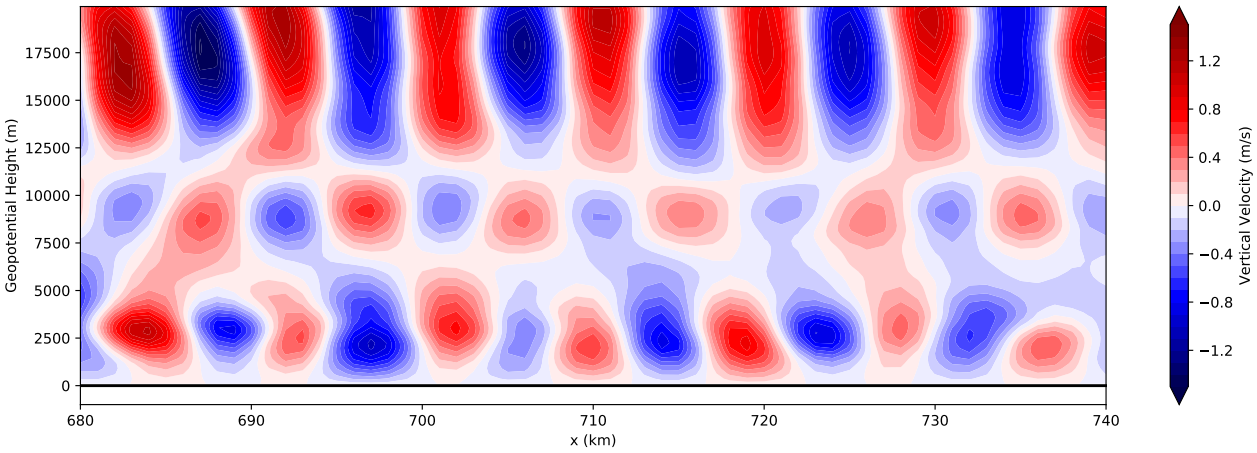

Figure 4.12: As in Fig. 4.2, but for the HHNL run at $y = 228$ km and $t = 10$ hr.

lower layer is much more irregular, which is consistent with interference from a superposition of wave modes.

4.2.3 HHIT Simulation

The HHIT simulation further supports the idea of a superposition of wave modes. Figures 4.13 and 4.14 show vertical velocity profiles of the idealized terrain run at 5 and 10 hours of integration. The corresponding figure to Fig. 4.10a, Fig. 4.13a, shows much more clearly the interference pattern characteristic of a superposition of wave modes. Both the cross mountain wave mode and the south-north wave modes are clearly present, and there are clear areas of both constructive and destructive interference. While the south-north mode seems to dominate even in the lower troposphere, this is easily explained by the terrain configuration. The south-north side ridges are positioned at multiples of the wavelength of the south-north wave mode. The resonance induced by this configuration serves to amplify the waves more than that of the realistic topography. It should be noted that the amplitudes of the waves are significantly weaker than in the HHFT and HHNL runs. However, the height of the IT terrain is much lower than that of either the FT or NL terrains (300 m vs. approximately 1100 m), and therefore the weaker amplitudes are to be expected.

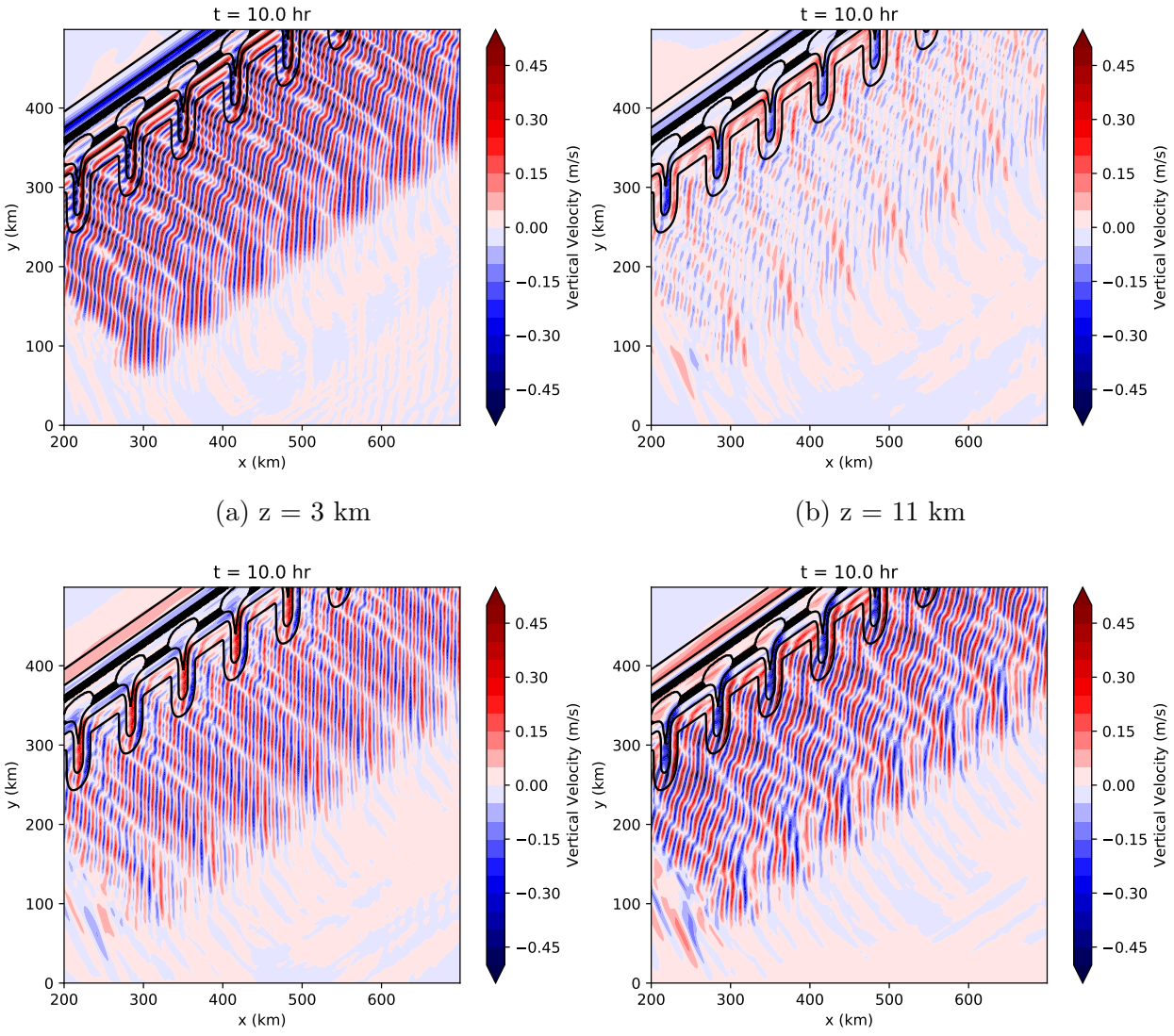

(a) z = 3 km

(b) z = 11 km

(c) z = 15 km

(d) z = 20 km

Figure 4.13: Vertical velocity at hour 5 of the HHIT run.

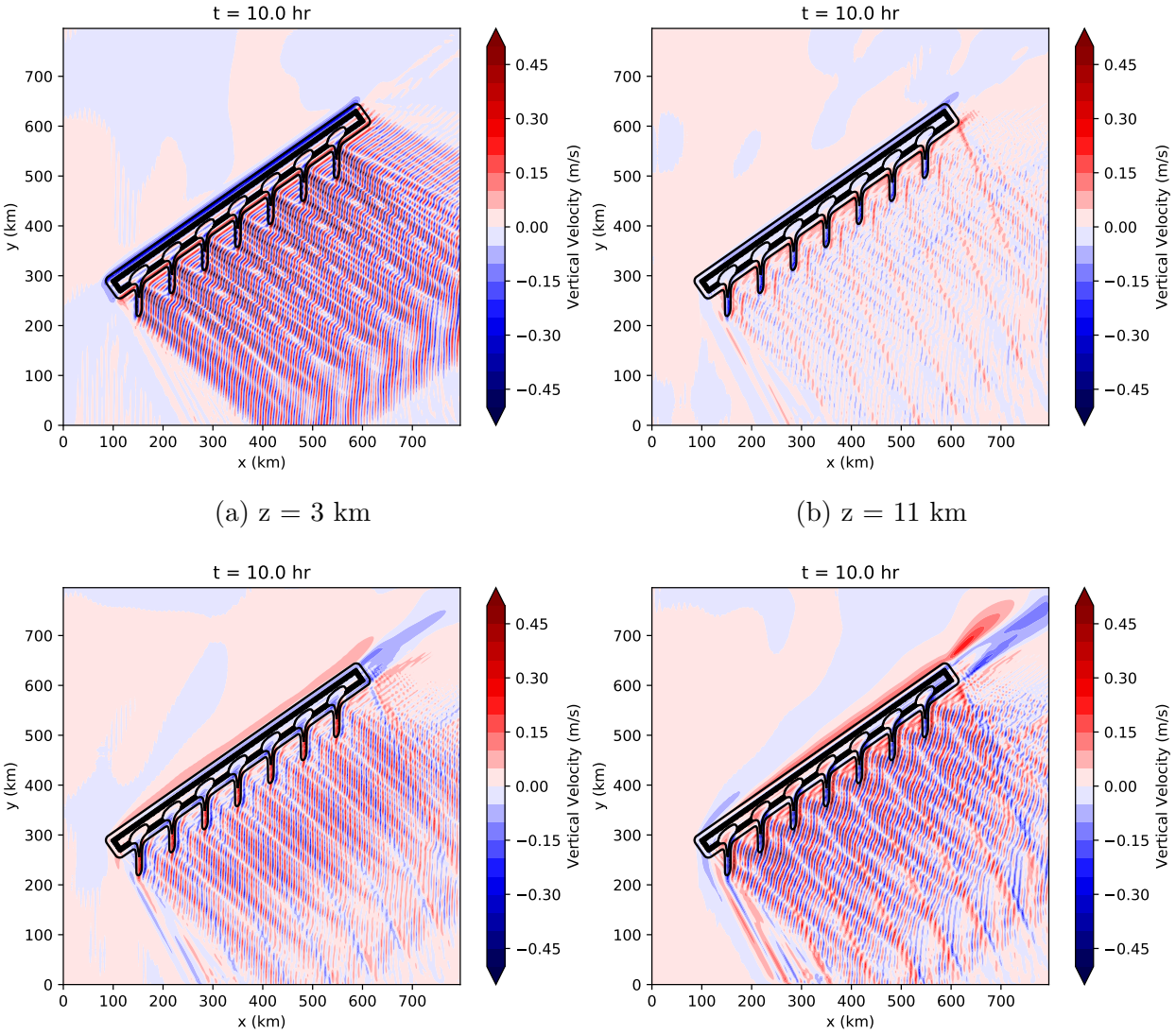

(a) z = 3 km

(b) z = 11 km

(c) z = 15 km

(d) z = 20 km

Figure 4.14: As in Fig. 4.13, but at hour 10.

.

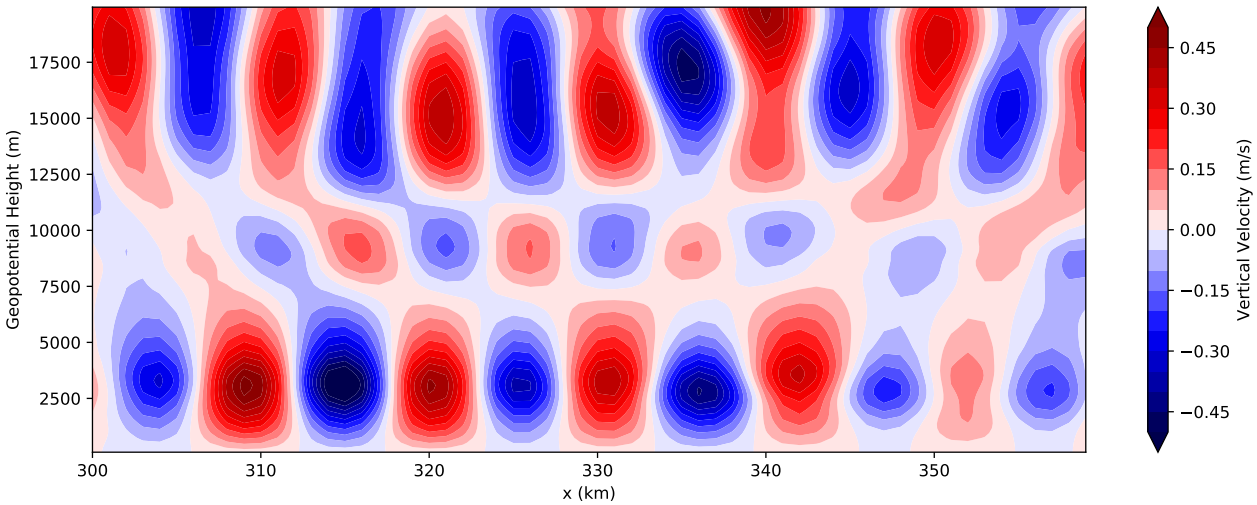

Figure 4.15: As in Fig. 4.2, but for the HHIT run at $y = 220$ km and $t = 10$ hr.

A west-east vertical cross section of the HHIT run (Fig. 4.15) shows a clear higher order trapped wave signature, especially from 312 to 345 km. There are two nodal lines at approximately 7500 and 11000 m. These nodal lines are located at different locations when compared to the FE runs. While both the FE cross sections (Figs. 4.2 and 4.4) and the HH cross section have a nodal line at 11 km, in the FE cross sections it is the lower nodal line while it is the upper nodal line in the HH cross sections. This may be an indication of a different trapped wave mode being generated in the HH cases as compared to the FE simulations.

4.3 Summary and Discussion

All 3D simulations reveal apparent higher-order trapped wave modes. However, the characteristics of the waves differ. The FE simulations appear to generate a wave mode with at least two nodal lines at altitudes of approximately 11 and 15 km. While there are potentially more nodal lines at lower altitudes, these are obscured by the presence of the cross-mountain trapped waves in the lower troposphere. In contrast, while the HH runs also produce higher-order modes, the nodal lines are lower, at altitudes of 7 and 11 km. The presence of a nodal

line at 11 km in both waves is unexplained, but it is perhaps coincidental.

Chapter 5

LINEAR EIGENVALUE SOLVER

The linear eigenvalue solver completes the theoretical investigation by finding eigenfunctions of the Fourier transform of the two-dimensional wave equation,

$$\frac{d^2\hat{w}}{dz^2} + \left(l^2 - k^2\right)\hat{w} = 0, \tag{5.1}$$

in cases where the Scorer parameter (l^2) is a certain function of height. Since the solver operates only in two-dimensions, it is necessarily to choose a wind direction from the full 3D wind field for input into the solver. In addition, the sounding must be further idealized in order to suit the constraints of the solver (described below). For the purposes of this study, two wind directions were chosen: the purely zonal wind (to analyze the transverse waves that appear to constitute the higher order stratospheric wave mode) and the wind direction approximately normal to the main ridge of the topography (the "cross-mountain" wind), to analyze the more conventional tropospheric trapped waves. Since the Southern Alps are oriented at an angle approximately 50° east of north, this wind was chosen to be 320° in meteorological wind direction (or −50° as an angle according to mathematical convention).

5.1 Description of Solver

The underlying algorithm for the linear eigenvalue solver is fully described in the appendix of Durran et al. (2015). The solver only considers background profiles for which the Brunt-Väisälä frequency (N) is piecewise constant with height and the wind speed U is piecewise linear with height. It then breaks up the profile into subdomains, each with constant N and linear U. The wave equation is then solved for an arbitrary horizontal wavenumber (k) within each subdomain, and both kinematic (velocity is continuous across the interface) and

dynamic (pressure is continuous across the interface) matching conditions are applied at the interface. However, for any given k, the matching condition will not necessarily be satisfied. If the residual of the equations governing the matching condition is less than a threshold value (specified in this work to be 10^{-8}), then the matching condition is determined to have been satisfied, and the solution is accepted as an eigenfunction of the wave equation for the given profile, with k as its accompanying eigenvalue.

As is noted in Durran et al. (2015), the mathematical method utilized by the numerical solver is fully generalizable to arbitrary continuous profiles of the Scorer parameter. However, in cases where the curvature term in the Scorer parameter (the second term in Eq. 2.15) is small, a layer approximation where the Scorer parameter varies linearly in each layer is a reasonable approximation to real atmospheric conditions. In addition, the layer approximation facilitates more direct comparison to previous theoretical studies, which typically employ this approximation to simplify the mathematical problem.

5.2 Input Profiles

The component of the wind in a certain direction is the projection of the wind vector onto a unit vector in the desired direction. A projection is defined by

$$\mathbf{v}' = (\mathbf{v} \cdot \mathbf{u})\,\mathbf{u}, \tag{5.2}$$

Where $\mathbf{v}$ is the vector to be projected, $\mathbf{u}$ is a unit vector in the desired direction, and $\mathbf{v}'$ is the projected vector. For our purposes, we are interested solely in the magnitude of the projection. Since $\mathbf{u}$ is a unit vector, the magnitude is simply $\mathbf{v} \cdot \mathbf{u}$ (Williams, 2014). A unit vector in any desired direction can be expressed in terms of its mathematical angle as $\langle \cos\theta, \sin\theta \rangle$. Then, if the components of the wind vector are defined as $\mathbf{v} = \langle u, v \rangle$, the magnitude of the projection is given by

$$\|\mathbf{v}'\| = u\cos\theta + v\sin\theta. \tag{5.3}$$

The components of the wind in the cross-mountain ($\theta = -55°$) and zonal ($\theta = 0°$) directions are shown in Fig. 5.1a and Fig. 5.1b, respectively. The blue line in each figure

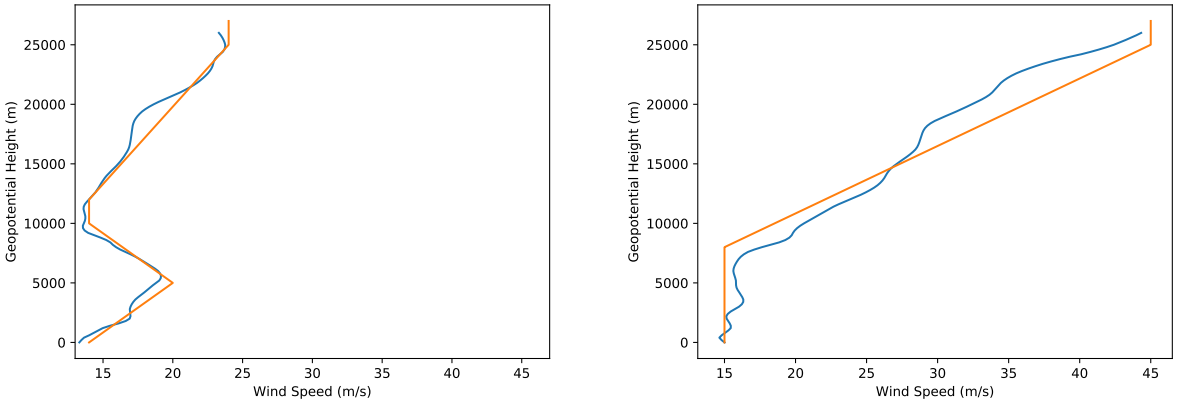

(a) Cross-mountain Wind

(b) Zonal Wind

Figure 5.1: Input wind profiles used for the eigenvalue solver. The relevant components from the HH runs are shown in blue, while the piecewise linear idealizations are shown in orange.

shows the projected wind field of the HH sounding. Since the eigenvalue solver requires the input wind to be piecewise linear, the fields were idealized as shown by the orange lines. Note that the magnitude of the zonal wind in the stratosphere is much greater than that of the cross-mountain wind.

The resulting Scorer parameter profiles are shown in Fig. 5.2. Above 11 km, the Scorer parameter decreases with height in both the cross-mountain and zonal wind profiles. This is consistent with the increase in wind speed in both profiles above 11 km. However, in the stratosphere, the Scorer parameter for the zonal cross section is consistently and substantially smaller in magnitude than for the cross-mountain profile. Therefore, the zonal wind is more favorable for wave trapping in the stratosphere than is the cross-mountain wind, and there is a possibility that the zonal wind may support modes that are not supported by the cross-mountain wind.

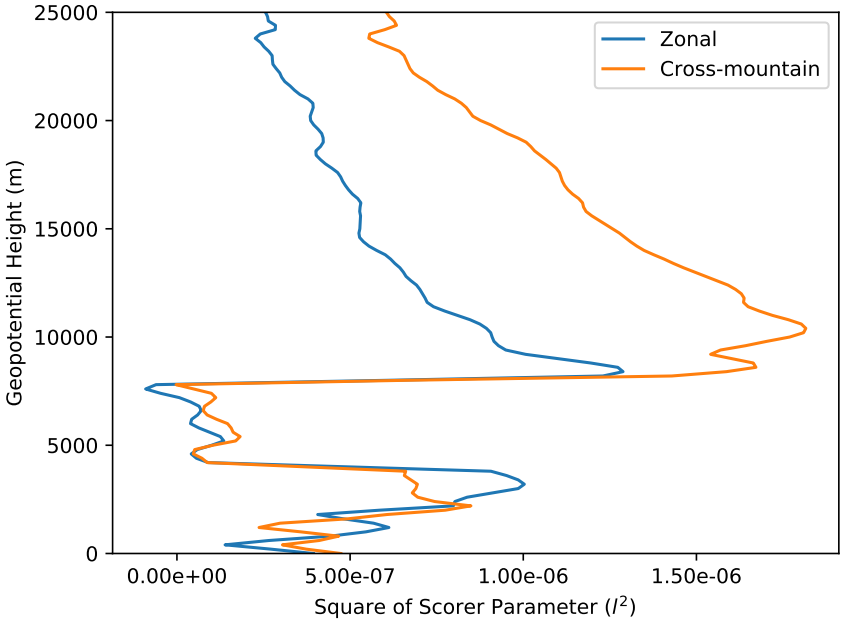

Figure 5.2: Vertical profiles of the Scorer parameter (Eq. 2.15) for the cross-mountain (orange) and zonal (blue) wind profiles.

5.3 Solver Results

The linear eigenvalue solver isolates the superposed wave modes and provides a clear explanation for the upper-level transverse waves. While the cross-mountain flow only supports one wave mode, the west-east wind supports multiple modes, including one with a maximum amplitude in the stratosphere. Since the modes are linear, the superposition principle applies. Therefore the expected total solution is a linear combination of the supported modes, which would explain why we see the expected behavior in the lower troposphere but transverse waves in the stratosphere.

5.3.1 Cross Mountain Flow

As stated above, the cross-mountain flow supports only one trapped wave mode (Fig. 5.3). This wave mode resembles a leaky trapped wave as shown in Durran et al. (2015), where the maximum is in the lower troposphere at a height of approximately 3 km. This is consistent with all model simulations, where the maximum amplitude of the wave occurs at approximately 3 km. It is expected that this wave mode would be dominant in the simulations with the real terrain and especially the NL terrain since the cross-mountain flow is normal to the primary axis of the topography. However, since the only supported wave mode has very little amplitude in the stratosphere, there is the potential for other wave modes to dominate in that region.

5.3.2 Zonal Flow

In contrast to the cross-mountain wind, the west-east wind supports three trapped wave modes (Fig. 5.4). Note that all three wave modes have nodal points at approximately 10 km. This, combined with the low amplitude of the cross-mountain wave mode at that altitude, explains the relatively small wave amplitudes at that altitude compared to both above and below.

Note also that the first and second supported modes have a maximum in the lower tropo-

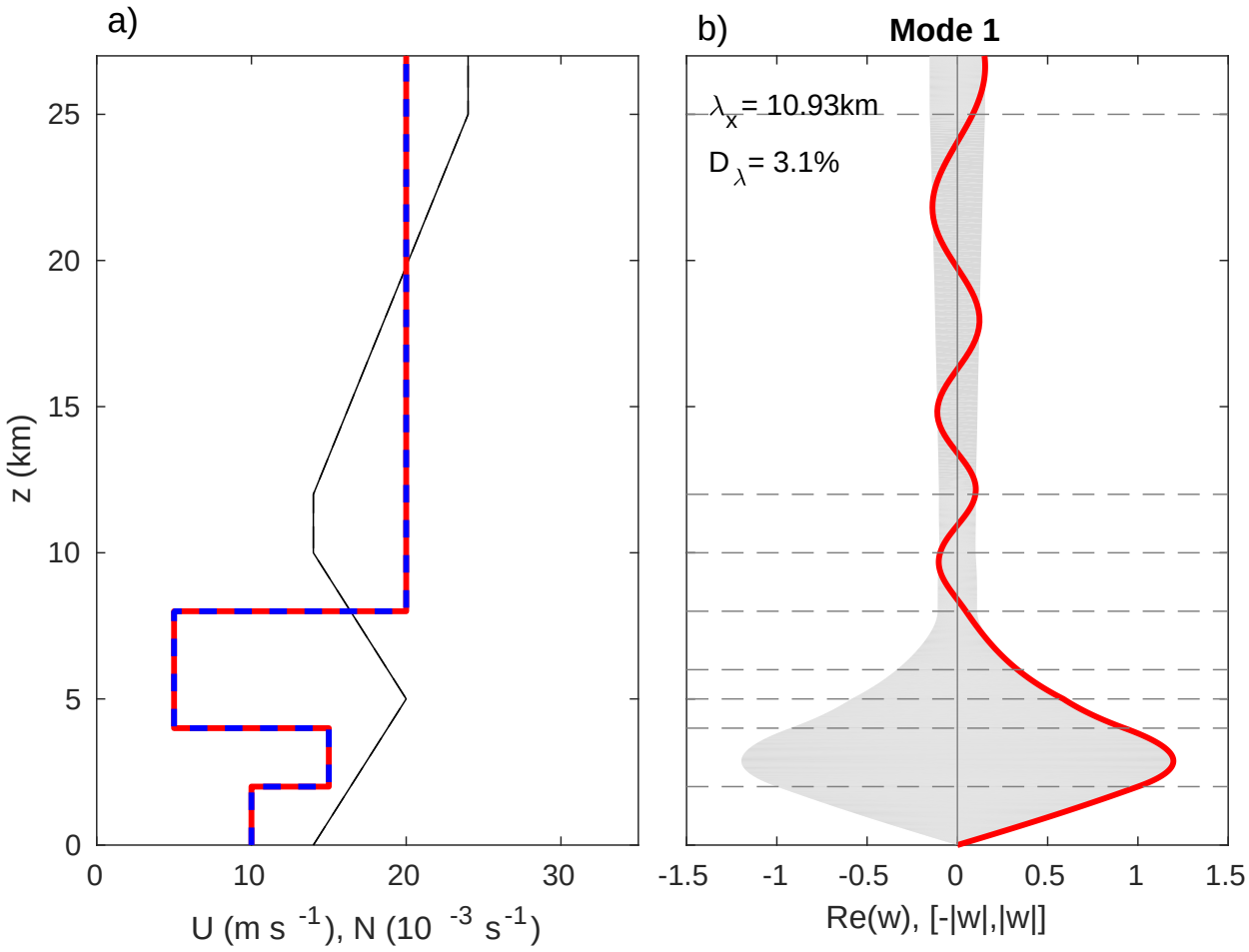

Figure 5.3: Results from the linear eigenvalue solver for the cross-mountain mode: the left panel shows the input wind speed (m/s, black) and Brunt-Väisälä frequency (10^{-3} s^{-1}, red and blue dashes). The right panel shows the vertical velocity profile with height for a phase with maximum amplitude. λ_x denotes the horizontal wavelength, while D_λ is the percentage of downstream dissipation per wavelength.

sphere, again around 3 km. Since these modes have extremely close wavelengths (8.71 km vs 8.93 km), these waves are essentially in phase for a large region downstream of the mountain. Therefore, these wave modes positively reinforce each other in the lower troposphere, and there should be large amplitude around 3 km. This is indeed easily seen in the idealized simulation with idealized terrain, where the waves appear to form a superposition of the cross-mountain mode and a transverse mode (Figs. 4.13a and 4.14a). In addition, note that above approximately 6 km, the waves largely exhibit deconstructive interference, as their vertical velocities are of opposite sign.

The third mode, however, exhibits significant differences from the first two and is what appears to explain the wave activity in the stratosphere. Unlike classical trapped wave modes, this mode has very little amplitude in the troposphere. It instead has its greatest amplitude in the stratosphere at approximately 17 km. While the idealized runs in Figs. 4.10-4.14 show an increase in wave amplitude with height above 14 km, consistent with this mode, it does not appear to have a maximum at 17 km. Instead the amplitude continues to increase up to 20 km. A possible explanation for this discrepancy results from a correction for compressibility effects, which is discussed in further detail in the next section.

5.4 Eigenfunction Generation in Compressible Simulations

It is important to note that the equation solved by the linear eigenvalue solver, Eq. 5.1, was derived using the Boussinesq approximation. However, all three-dimensional model simulations in Ch. 4, as well as the real atmosphere itself, are compressible. Therefore, it is important to determine whether or not these modes can indeed be generated in a fully compressible framework. To do this, two-dimensional simulations using the meso12 model, developed at the University of Washington, were performed.

5.4.1 meso12 Model Description

The core numerics and dynamics of the model are described in Durran and Klemp (1983). The model is fully compressible and nonhydrostatic. While meso12 has the capability to

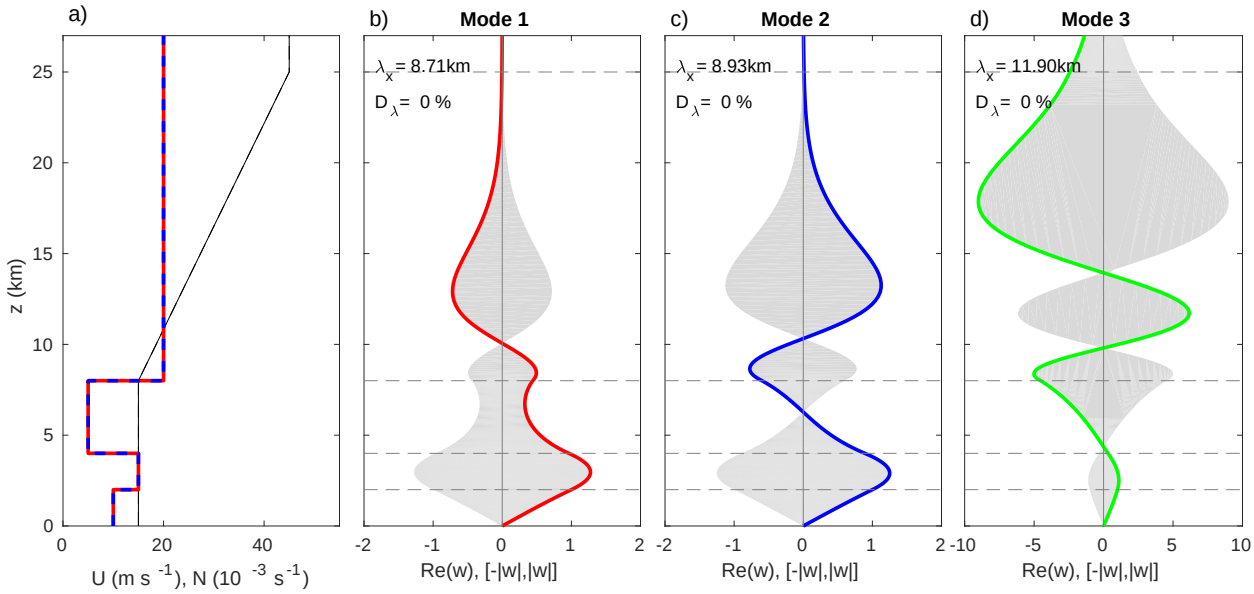

Figure 5.4: As in Fig. 5.3, but for the zonal wind.

include moisture effects, for the purposes of this study it is constrained to dry dynamics.

5.4.2 Terrain Description

The lower boundary condition for the two-dimensional idealized runs is significant as it is the source of the forcing for the waves. The lower boundary condition was chosen to be five periods of a cosine ridge with a wavelength equal to that of the desired mode,

$$h(x) = \frac{h_0}{2} \cos\left(\frac{2\pi}{\lambda} x\right) + \frac{h_0}{2}, \tag{5.4}$$

where h_0 is the mountain height and λ is the wavelength. This specific boundary condition cleanly and efficiently forces the desired mode and allowed us to verify that the mode is indeed supported in a compressible numerical solution.

5.4.3 meso12 Model Results

Two-dimensional meso12 simulations demonstrate that the modes computed by the linear eigenvalue solver can indeed be generated in a fully numerical model. The results after the

simulations were integrated to steady state are shown in Fig. 5.5. Figure 5.5a shows vertical velocity from the simulation with terrain with a 9 km wavelength, while Fig. 5.5b shows vertical velocity from the simulation with 12 km wavelength terrain. To better compare these modes to the results from the eigenvalue solver, vertical profiles were taken at 292 km from the 9 km run and 515 km from the 12 km run. These profiles are shown in Fig. 5.6.

While the first mode is qualitatively fairly well generated in Fig. 5.6a, the stratospheric maximum is noticeably stronger than the tropospheric maximum, in contrast to the mode from the eigenvalue solver. This may be due to a couple of factors. First, the density effect leads to an increase in amplitude with height in a compressible atmosphere. Since the eigenvalue solver is Boussinesq, the density effect does not occur, and so it would be expected that the amplitude is increasingly underestimated by the Boussinesq solution as the height increases. Secondly, since the first and second modes have extremely similar wavelengths, it is probable that both modes were forced in this simulation. If, however, the two modes were about 180° out of phase, the stratospheric maximum would be reinforced while the tropospheric maximum would decrease in magnitude. The two modes can be isolated using a linear least squares analysis, as is discussed in the section below.

Since the third mode has a substantially longer wavelength than the first two modes, it is much easier to generate and analyze in isolation, as is shown in Fig. 5.6b. To facilitate comparison with the Boussinesq solution of the linear eigenvalue solver, the density effect is compensated for by multiplying by a factor $\left(\frac{\rho(z)}{\rho_0}\right)^{1/2}$, where $\rho(z)$ is the density at the height in question, and ρ_0 is the density at the surface. The result of this calculation is shown in Fig. 5.7. Since the maximum amplitude (but not the amplitude profile) output from the eigenvalue solver is arbitrary, the modes have been normalized to have the same value for the maximum amplitude. As can be seen in Fig. 5.7, the agreement between the fully-numerical compressible model and the linear eigenvalue solver is quite good, which lends confidence to the applicability of the results from the eigenvalue solver to fully numerical simulations.

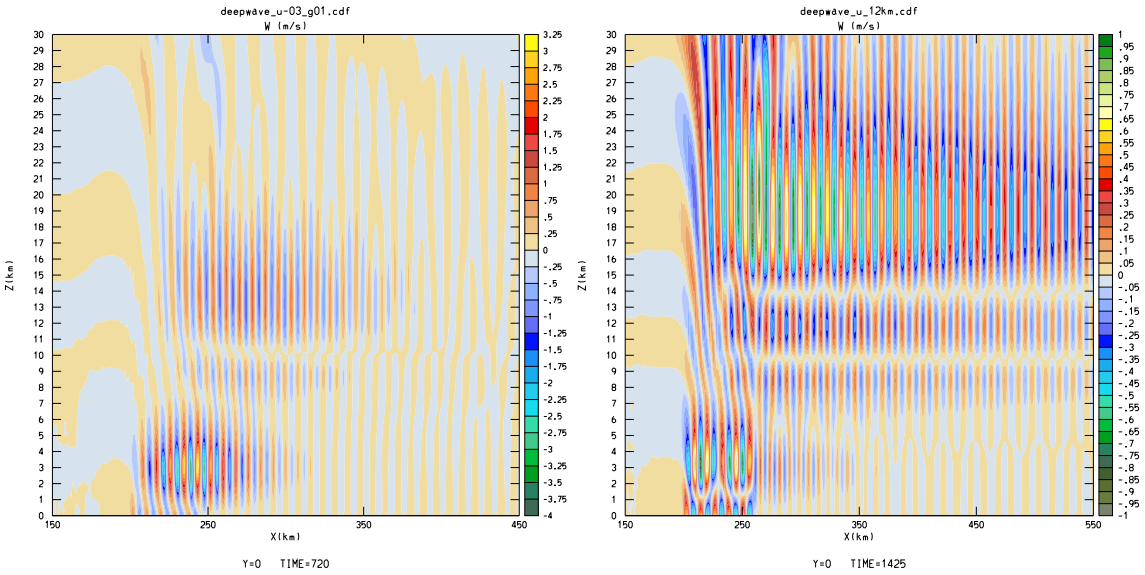

(a) 9 km (b) 12 km

Figure 5.5: Vertical velocity for the two-dimensional simulations after integration to approximately steady state, which occurs at $t = 720$ min for the 9 km simulation and $t = 1425$ min for the 12 km simulation.

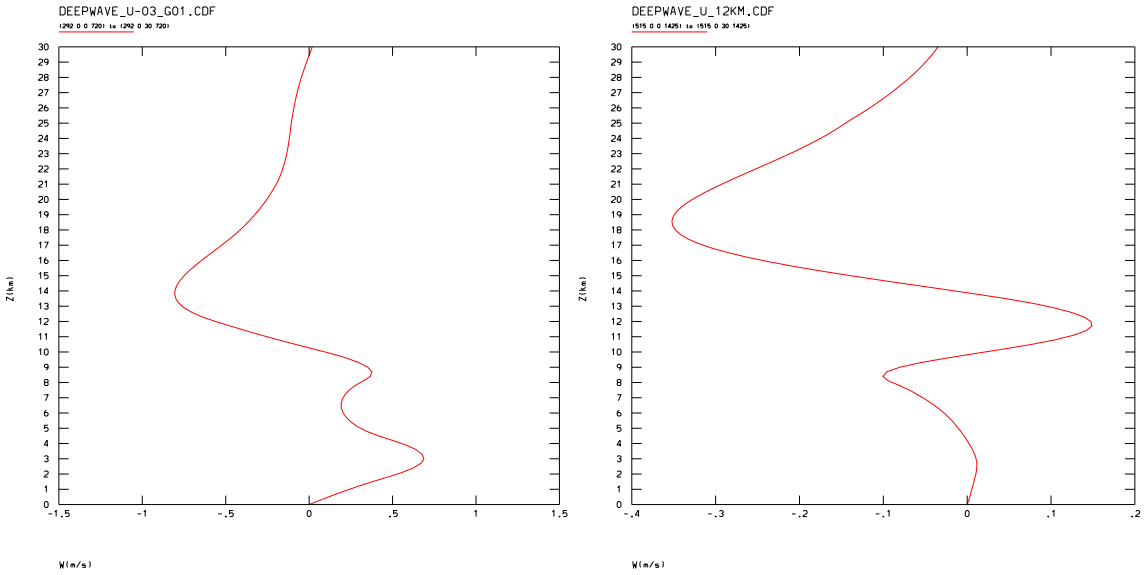

(a) 9 km (b) 12 km

Figure 5.6: One-dimensional vertical cross sections of the vertical velocity plots from Fig. 5.5. The left cross section was taken at $x = 292$ km of Fig. 5.5a, and the right cross section was taken at $x = 515$ km of Fig. 5.5b.

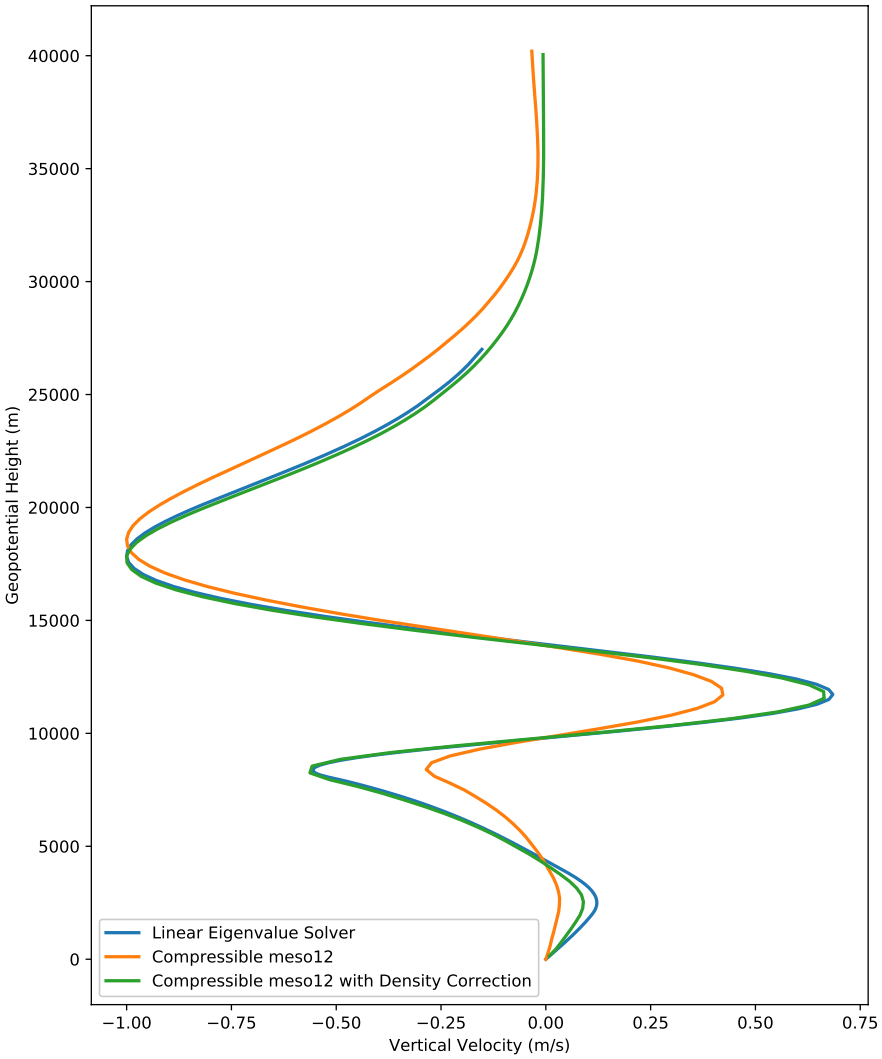

Figure 5.7: Quantitative comparison of the third wave mode output from the linear eigenvalue solver in Fig. 5.4 and the wave mode from the 12 km wavelength two-dimensional compressible simulation in Fig. 5.6b. Both profiles are normalized to have a maximum amplitude of unity. The result from the linear eigenvalue solver is shown in blue, while the result from the two-dimensional simulation is shown in orange. The same profile from the model, when adjusted to remove the density effect, is shown in green.

5.4.4 Linear Least Squares Analysis

The two modes believed to be generated in the simulation shown in Figs. 5.5a and 5.6a can be isolated through the use of a linear least squares analysis. This type of analysis represents a given function $f(x)$ in terms of basis functions $u_1(x), u_2(x), ..., u_n(x)$, such that

$$f(x) = c_1 u_1(x) + c_2 u_2(x) + ... + c_n u_n(x) + \epsilon(x), \tag{5.5}$$

where $c_1, c_2, ..., c_n$ are constants and ϵ is a function known as the "residual". The goal of linear least squares analysis is to minimize this residual (Trefethen and Bau, 1997).

To apply linear least squares analysis to our problem, we first consider that the given eigenfunctions are functions solely of z. Then, we can apply the least squares analysis at each horizontal point. In this case, while the basis functions are unchanging, the "constants" become functions of x, such that

$$w(x, z) = c_1(x) w_1(z) + c_2(x) w_2(z) + \epsilon(x, z), \tag{5.6}$$

where $w_1(z)$ and $w_2(z)$ are the first and second eigenfunctions in Fig. 5.4 (with adjustments made as above to compensate for the density effect), and $w(x, z)$ is the output vertical velocity field from meso12 at a given time.

The results from the least squares analysis are shown in Figs. 5.8 and 5.9. The coefficients, shown in Fig. 5.8, have a functional form of a sinusoid multiplied by an envelope function. This is consistent with expectations. The x structure of the mode should be sinusoidal, as a Fourier transform in x was applied to derive Eq. 5.1 and the wavenumber k was then fixed. The envelope function can be plausibly explained by dissipation of the numerical solution.

The wavelengths of the two modes in the least squares regression are approximately 8.1 km and 8.5 km, respectively. These values are both shorter than the values from the eigenvalue solver, which were 8.71 and 8.93 km (Fig. 5.4). One potential explanation is due to the 1 km resolution used in the numerical simulation, which, while small enough to resolve the waves with reasonable accuracy, may not be small enough to completely represent the

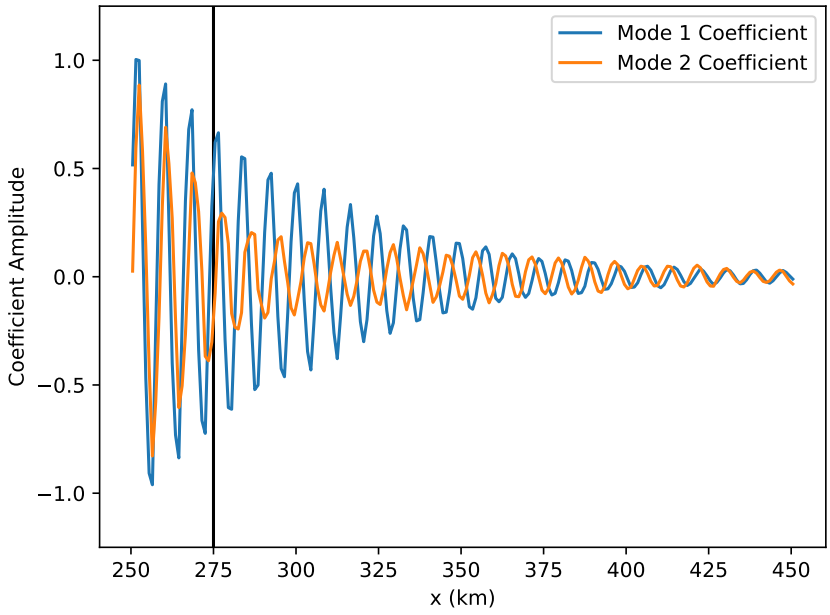

Figure 5.8: Coefficients of the least-squares regression. The blue line corresponds to the amplitude of mode 1 in Fig. 5.4, while the orange line corresponds to the amplitude of mode 2 in Fig. 5.4. The black line corresponds to the beginning of the region where residuals are qualitatively small (see Fig. 5.9).

correct wavelength. Regardless, further investigation is required to resolve the discrepancy between the regressed and predicted wavelengths.

Figure 5.9 reveals that there is an initial region of large residuals, followed by relatively flat and constant residuals for the rest of the domain. This is perhaps an indication of a region of vertically propagating waves within the first 25 km of the regression. In addition, since the numerical solution is never truly steady-state, there are some errors introduced when comparing to the steady-state solution, which may be more apparent closer to the forcing region.

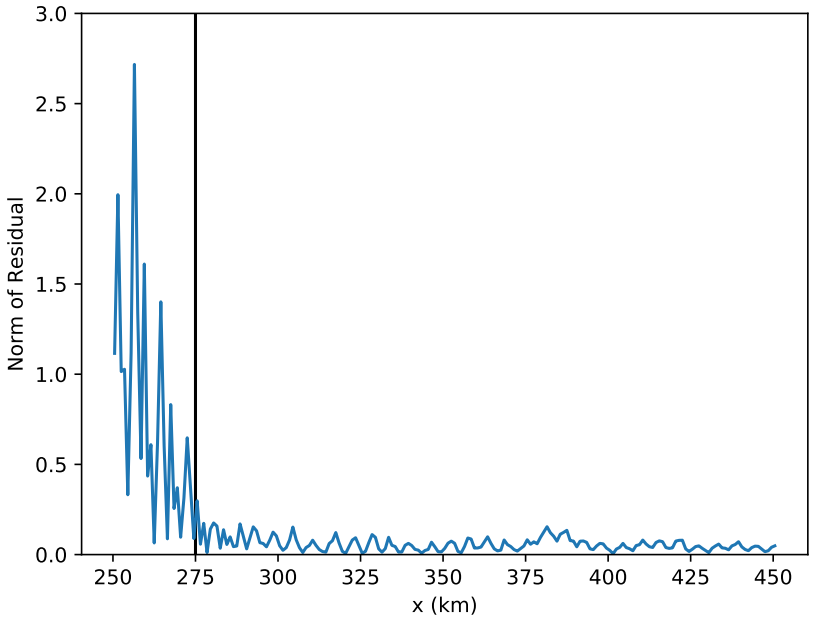

Figure 5.9: Norm of the residual vector of the least squares regression. The black line denotes a qualitative boundary between residuals with large magnitude and those with small magnitude.

Chapter 6

SUMMARY AND CONCLUSIONS

Model simulations ranging from the most fully realistic to the most fully idealized appear to generate higher-order trapped wave modes for the 28 July 2014 case over the Southern Alps of New Zealand. These wave modes, in contrast to typical trapped waves, are not oriented along the topography, which in New Zealand is from southwest to northeast, as is usual for trapped waves, but are instead oriented from south to north. In addition, these higher-order modes appear to attain their maximum amplitude in the stratosphere instead of the lower troposphere.

In the most fully-realistic simulations (the FE simulations), the higher-order trapped modes appear to have at least three nodal lines at approximately 9, 11 km, and 16 km. In contrast, the idealized simulations (HH simulations) have only two nodal lines, which are located at approximately 7 km and 11 km. For an idealized atmospheric structure reminiscent of the actual atmospheric conditions on 28 July, a linear eigenvalue solver finds three wave modes, all of which have at least one node, which matches the criterion for a higher-order wave mode. The second mode from the eigenvalue solver has nodal points at altitudes matching that of the waves from the HH runs, while the third mode from the solver has nodes matching those from the FE runs. While it appears that the HH simulations are triggering a different mode than the FE simulations, it is nonetheless encouraging to see both modes represented in the eigenvalue solver results.

In contrast to the three south-north trapped wave modes supported by the zonal wind, the cross-mountain wind only supports one trapped wave mode, which like classical trapped waves has its maximum in the lower troposphere. This is due to the strong westerly wind component at high altitudes. Due to the inverse relation between wind speed and the Scorer

parameter, this strong wind component results in a large enough change in the Scorer parameter to trap waves in the stratosphere. However, the Scorer parameter in the cross-mountain direction does not decrease strongly enough to trap waves in that orientation.

While the eigenvalue solver indicates that the south-north modes also have some amplitude in the lower troposphere, the FE simulations do not appear to show a distinct signature of this. However, the third wave mode from the eigenvalue solver has very little amplitude in the lower troposphere than in the stratosphere. Since even without compensating for the density effect the south-north waves are weaker in the stratosphere than the cross-mountain waves are in the lower troposphere, it stands to reason that the cross-mountain wave signal is simply too strong and dominates such that the south-north waves are essentially invisible, although present, in the lower troposphere. In the HH modes, however, a superposition of wave modes is clearly visible. The mode from the eigenvalue solver that most closely matches that of the HH runs is the second wave mode, which has more amplitude in the troposphere than the third mode.

These simulations provide evidence that higher-order wave modes can be supported in the actual atmosphere. However, work remains to look for signatures of these higher-order modes in observational datasets. The DEEPWAVE campaign resulted in a wealth of data from multiple observational platforms, several of which conducted measurements in the stratosphere. While most of these platforms were removed prior to the case day in question in this study, the potential exists that other DEEPWAVE cases may also have atmospheric structures that support higher-order trapped wave modes.

BIBLIOGRAPHY

Corby, G. A., and C. E. Wallington, 1956: Airflow over mountains: The lee-wave amplitude. *Quarterly Journal of the Royal Meteorological Society*, **82 (353)**, 266–274, doi:10.1002/qj.49708235303, URL http://onlinelibrary.wiley.com/doi/10.1002/qj.49708235303/abstract.

Danielsen, E. F., and R. Bleck, 1970: Tropospheric and Stratospheric Ducting of Stationary Mountain Lee Waves. *Journal of the Atmospheric Sciences*, **27 (5)**, 758–772, doi:10.1175/1520-0469(1970)027⟨0758:TASDOS⟩2.0.CO;2, URL https://journals.ametsoc.org/doi/abs/10.1175/1520-0469(1970)027%3C0758%3ATASDOS%3E2.0.CO%3B2.

Durran, D. R., 1981: The Effects of Moisture on Mountain Lee Waves. Ph.D. thesis, Massachusetts Institute of Technology.

Durran, D. R., 1990: Mountain Waves and Downlope Windstorms. *Meteorological Monographs*, **23 (45)**, 59–81.

Durran, D. R., M. O. G. Hills, and P. N. Blossey, 2015: The Dissipation of Trapped Lee Waves. Part I: Leakage of Inviscid Waves into the Stratosphere. *Journal of the Atmospheric Sciences*, **72 (4)**, 1569–1584, doi:10.1175/JAS-D-14-0238.1, URL http://dx.doi.org/10.1175/JAS-D-14-0238.1.

Durran, D. R., and J. B. Klemp, 1982: The Effects of Moisture on Trapped Mountain Lee Waves. *Journal of the Atmospheric Sciences*, **39 (11)**, 2490–2506, doi:10.1175/1520-0469(1982)039⟨2490:TEOMOT⟩2.0.CO;2, URL http://journals.ametsoc.org/doi/abs/10.1175/1520-0469%281982%29039%3C2490%3ATEOMOT%3E2.0.CO%3B2.

Durran, D. R., and J. B. Klemp, 1983: A Compressible Model for the Simulation of Moist Mountain Waves. *Monthly Weather Review*, **111 (12)**, 2341–2361,

doi:10.1175/1520-0493(1983)111⟨2341:ACMFTS⟩2.0.CO;2, URL http://journals.ametsoc.org/doi/abs/10.1175/1520-0493(1983)111%3C2341:ACMFTS%3E2.0.CO%3B2.

Eliassen, A., and E. Palm, 1960: Wave energy transfer in stationary gravity waves. *Geofys. Publ.*, **22 (3)**.

Fritts, D. C., and Coauthors, 2015: The Deep Propagating Gravity Wave Experiment (DEEPWAVE): An Airborne and Ground-Based Exploration of Gravity Wave Propagation and Effects from Their Sources throughout the Lower and Middle Atmosphere. *Bulletin of the American Meteorological Society*, **97 (3)**, 425–453, doi:10.1175/BAMS-D-14-00269.1, URL http://journals.ametsoc.org/doi/full/10.1175/BAMS-D-14-00269.1.

Gill, A. E., 1982: *Atmosphere-Ocean Dynamics*, International Geophysics Series, Vol. 30. Academic Press.

Jiang, Q., J. D. Doyle, A. Reinecke, R. B. Smith, and S. D. Eckermann, 2012: A Modeling Study of Stratospheric Waves over the Southern Andes and Drake Passage. *Journal of the Atmospheric Sciences*, **70 (6)**, 1668–1689, doi:10.1175/JAS-D-12-0180.1, URL http://journals.ametsoc.org.offcampus.lib.washington.edu/doi/abs/10.1175/JAS-D-12-0180.1.

Lyra, v. G., 1940: ber den Einflu\s s von Bodenerhebungen auf die Strmung einer stabil geschichteten Atmosphre. *Beitr. Phys. frei. Atmos*, **26**, 197–206.

Markowski, P., and Y. Richardson, 2010: *Mesoscale Meteorology in Midlatitudes*. Advancing Weather and Climate Science, Wiley.

Palm, E., and R. S. Scorer, 1958: Airflow over mountains: Indeterminacy of solution. *Quarterly Journal of the Royal Meteorological Society*, **84 (362)**, 464–466.

Petty, G. W., 2008: *A First Course in Atmospheric Thermodynamics*. Sundog Publishing.

Queney, P., 1948: The Problem of Air Flow Over Mountains: A Summary of Theoretical

Studies. *Bulletin of the American Meteorological Society*, **29 (1)**, 16–26, URL http://www.jstor.org/stable/26257649.

Queney, P., G. A. Corby, N. Gerbier, H. Koschmeider, and J. Zierep, 1960: The Airflow Over Mountains. Technical Note 34, World Meteorological Organization, 148 pp.

Scorer, R., 1949: Theory of waves in the lee of mountains. *Quart. J. Roy. Meteor. Soc.*, **75**, 41–56.

Skamarock, W., J. Klemp, J. Dudhia, D. Gill, D. Barker, W. Wang, X.-Y. Huang, and M. Duda, 2008: A Description of the Advanced Research WRF Version 3. NCAR Tech. Note NCAR/TN-475+STR, 113 pp. doi:10.5065/D68S4MVH.

Smith, R. B., B. K. Woods, J. Jensen, W. A. Cooper, J. D. Doyle, Q. Jiang, and V. Grubii, 2008: Mountain Waves Entering the Stratosphere. *Journal of the Atmospheric Sciences*, **65 (8)**, 2543–2562, doi:10.1175/2007JAS2598.1, URL http://journals.ametsoc.org/doi/full/10.1175/2007JAS2598.1.

Trefethen, L., and D. Bau, III, 1997: *Numerical Linear Algebra*. Society for Industrial and Applied Mathematics, Philadelphia.

Vadas, S. L., D. C. Fritts, and M. J. Alexander, 2003: Mechanism for the Generation of Secondary Waves in Wave Breaking Regions. *Journal of the Atmospheric Sciences*, **60 (1)**, 194–214, doi:10.1175/1520-0469(2003)060⟨0194:MFTGOS⟩2.0.CO;2, URL https://journals.ametsoc.org/doi/abs/10.1175/1520-0469%282003%29060%3C0194%3AMFTGOS%3E2.0.CO%3B2.

Williams, G., 2014: *Linear Algebra with Applications*. 8th ed., Jones & Bartlett Learning Series in Mathematics, Jones & Bartlett Learning, Burlington, Massachusetts.